Journal of Intelligent Manufacturing
https://doi.org/10.1007/s10845-024-02349-8

A novel curved surface profile monitoring approach based on geometrical-spatial joint feature

Yiping Shao[1] · Jun Chen[1] · Xiaoli Gu[2] · Jiansha Lu[1] · Shichang Du[3]

Received: 23 August 2023 / Accepted: 12 February 2024
© The Author(s), under exclusive licence to Springer Science+Business Media, LLC, part of Springer Nature 2024

Abstract
With the development of high-end manufacturing, a variety of sophisticated parts with complex curved surfaces have emerged, and curved surface profile monitoring is of great importance for achieving the higher performance of a part. Benefiting from the recent advancements in non-contact measurement systems, millions of high-density point clouds are rapidly collected to represent the entire curved surface, which can reflect the geometrical and spatial features. The traditional discrete key quality characteristics-based monitoring approaches are not capable of handling complex curved surfaces. A novel curved surface profile monitoring approach based on geometrical-spatial joint features is proposed, which consists of point cloud data preprocessing, Laplace–Beltrami spectrum calculation, spatial geodesic clustering degree definition, and multivariate control chart construction. It takes full advantage of the entire wealth information on complex curved surfaces and can detect the small shifts of geometrical shape and spatial distribution information of non-Euclidean surfaces. Two real-world engineering surfaces case studies illustrate the proposed approach is effective and feasible.

Keywords Curved surface · Profile monitoring · Geometrical feature · Spatial distribution · Non-Euclidean surfaces

Introduction

With the development of high-end manufacturing, it appears a large number of high-precision and high-added value parts with complex curved surfaces, such as turbine rotor and blade, cylinder head combustor chambers of automobile engines, and vacuum chambers of semiconductor equipment. The surface profile quality of these parts is of great importance for the functional behavior of a part including stiffness, abrasion-resistance, reliability and life (He et al., 2019; Moreira et al., 2019). It depends on the stability of the manufacturing process, the profile error will fluctuate greatly when the manufacturing process is unstable, thereby leading to product failure or inaccurate assembly. For example, in the manufacturing process of engine cylinder bore, due to the vertical and rotary motion of honing head, which leads to deviations between the actual profile of the cylinder and the standard profile (roundness, cylindricity). The profile deviations seriously affect the sealing, reliability and life of the engine cylinder bore. Therefore, it is necessary to measure the processed surface profile, and the deviation between the actual machined surface and the standard surface is modeled and analyzed. Finally, the surface profile monitoring of the engine cylinder hole is realized by monitoring the model parameters and error terms (Zhao et al., 2020). For the combustion chamber of engine cylinder head, it is composed of complex curved surfaces with intersecting holes, and the inner surface is cast by mold. At the same time, the milling depth of the bottom surface of the cylinder head will

✉ Jiansha Lu
ljs@zjut.edu.cn

Yiping Shao
syp123gh@zjut.edu.cn

Jun Chen
2112102402@zjut.edu.cn

Xiaoli Gu
guxiaoli@zhejianglab.com

Shichang Du
lovbin@sjtu.edu.cn

1 College of Mechanical Engineering, Zhejiang University of Technology, Hangzhou 310023, China

2 Zhejiang Lab, Hangzhou 311121, China

3 School of Mechanical Engineering, Shanghai Jiao Tong University, No. 800 Dongchuan Road, Shanghai 200240, China

Published online: 25 March 2024

affect the shape of the curved surface, which also determines the volume of the combustion chamber, thereby affecting the performance of the engine. Therefore, the processed cylinder head combustion chamber is measured to obtain the surface profile data. By monitoring the surface profile quality in the manufacturing process, the cylinder head manufacturing problems can be found in time (Zhao et al., 2023a, 2023b). In the manufacturing process of wafers, silicon ingots are usually cut into several sections using a wire saw. After several flattening steps such as grinding, polishing and cleaning, the wafers are sent to the front-end and back-end processes, and the final chip is obtained. In the front-end process, unsatisfactory geometric surface profile quality often leads to a large number of defective chips on the wafer, resulting in manufacturing process delays and economic losses. For the processed wafer, the machining error in actual manufacturing process is determined by qualifying the geometric profile deviation between the actual wafer and the standard wafer, and checking whether the newly produced wafer meets the standards. By monitoring the surface profile quality of the part and eliminating the influence of random errors, it facilitates the traceability of errors in the manufacturing process and improves the stability of the machining process. Therefore, the surface profile quality monitoring method proposed in this paper is of great significance for the manufacturing process of complex surfaces (Zhang et al., 2016). According to the difference in geometrical properties, the engineering workpiece surfaces can divide into Euclidean surfaces and non-Euclidean surfaces (Jiang et al., 2021). The Gaussian curvature of the Euclidean surface is zero everywhere and it usually appears as a plane or a cylinder, while the non-Euclidean surface appears as curved surfaces with non-zero and variable Gaussian curvature including a sphere surface or a freeform surface. The non-Euclidean surfaces have complex structures and arbitrary shapes, which exist widely in engineering practice. The traditional contact measurement approach can only obtain the three-coordinate information of limited measurement points, which is difficult to characterize complex non-Euclidean surfaces. Benefiting from the recent advancements in non-contact measurement systems, millions of high-density point clouds are rapidly collected for the complex manufacturing process (Shao et al., 2021; Zhao et al., 2023a, 2023b). They can represent a total part's surface with high fidelity and high-density (HD) datasets in the forms of point clouds, which achieve the high-definition reproduction of the surface profile and offer new opportunities to monitor the small shifts of the surface geometry. The resulting high-density datasets not only have a great potential to inspect parts clearly, but also bring challenges to quality monitoring of parts. Unfortunately, traditional monitoring approaches have yet to be adapted to take full information of the new data-rich condition.

Statistical control chart is a powerful tool in surface quality monitoring, which determines the stability of the manufacturing process by analyzing the surface quality of the parts produced in the stable state. Many researchers have proposed a large body of profile monitoring works based on image data and point cloud data by using control charts. Depending on the different kinds of surfaces, the monitoring strategies are also divided into two categories. As for Euclidean surfaces, Megahed et al. (2012) developed an extended likelihood ratio control chart based on a spatiotemporal framework to monitor image data. He et al. (2016) proposed a multivariate generalized likelihood ratio (MGLR) control chart to monitor grayscale images of industrial products. Zhang et al. (2016) proposed an Additive Gaussian Process model to approximate a standard geometric profile of a wafer, and quantified the spatially correlated deviations in an in-control manufacturing process. Shang et al. (2019) presented an intrinsic Gaussian Markov random field (IGMRF) with the hierarchical Bayesian model for modeling 2D spatial count data, and developed a multivariate exponentially weighted moving average (MEWMA) control chart to monitor wafer quality and detect out-of-control wafers. Suriano et al. (2015) proposed a modeling and monitoring method for surface variation control by fusing cross-correlations among the measured data and manufacturing process variables along with spatial correlations. Dastoorian and Wells (2023) developed a hybrid offline/online quality control framework for real-time monitoring high-density data sets which is fused by images and point cloud data. Zhao et al. (2020) proposed a circular and cylindrical profile monitoring approach considering spatial correlations. Wang et al. (2016) developed a control chart based on a generalized likelihood ratio to rapidly detect process faults and provide diagnostic information for process improvement. Huang et al. (2021) simulated the average displacement of defects in different positions, sizes, and amplitudes of parts by constructing a control chart. Wang et al. (2014) proposed a Gaussian-Kriging model based control chart to monitor the machining process for a two-dimensional surface profile of products. Li et al. (2022) proposed a time-domain spectral analysis method based on grinding force signal and grinding surface texture curve to realize real-time monitoring of ceramic surface roughness during the grinding process.

Compared to the Euclidean surface, the non-Euclidean surface is characterized by three-dimensional high-density point cloud data containing spatial information and the geometrical shape, which is difficult to be parameterized. The traditional discrete key quality characteristics based-monitoring approaches for Euclidean surfaces are not capable of handling these high-density point clouds, which cannot be directly applied to non-Euclidean surfaces. There are few studies on non-Euclidean surface profile monitoring. Based on point cloud data, Wells et al. (2016, 2021) proposed

adaptive generalized likelihood ratio (AGRL) and Non-Uniform Rational Basis Spline (NURBS) surface approach to statistically monitor manufacturing processes respectively. According to the similarity between the probability density function of the observed surface and the normal surface, Baek et al. (2023) proposed a new method to monitor the shifts in multimode surface topography. Colosimo et al. (2014) proposed a Gaussian process modeling approach to model manufacturing surfaces, and monitor deviations between the actual surface and the target surface using the Hotelling T^2 control chart. Instead of charting summary statistics, Wang and Tsung (2005) proposed charting schemes based on the quantile–quantile (Q–Q) plot and described various shift patterns in a huge sample using different profile monitoring methods. Bui and Apley (2022a, 2022b), Zhang et al. (2023) proposed a manifold learning method to characterize the shape deviation fluctuation between parts. Ren and Ni (2021) proposed a real-time monitoring framework for the wafer manufacturing process, the statistics of T^2, SPE and C were calculated to achieve the process control. Li et al. (2020) proposed a new multivariate nonparametric control chart based on running tests for multivariate data stream monitoring.

However, these current profile monitoring researches on the non-Euclidean surface still have their limitations. The mapping-based dimension-reduction methods are easy to lose important spatial data of deviation position, and the process modeling methods are only suitable for parametric surfaces. Moreover, the time-consuming point cloud registration between the actual surface and the nominal surface before monitoring, which does not meet the requirement of production takt. More recently, Zhao and Castillo (2021, 2022) proposed a registration-free approach based on the Laplace–Beltrami spectrum to monitor the shape variation, but it ignores the spatial distribution information of the point cloud. Therefore, the main contribution of this paper is that a novel curved surface profile monitoring approach based on the geometrical-spatial joint features is presented. As an inherent measure of the three-dimensional surface manifold, the Laplace–Beltrami spectrum is developed to characterize the shape information of the curved surface, which is invariant with respect to rigid transformations of parts, thereby avoiding time-consuming registration with the nominal part. A new index called spatial geodesic clustering degree based on spatial geodesic distance matrix is defined, which can well represent the spatial distribution information of curved surfaces. A joint multivariate statistic LS-T^2 consists of Laplace–Beltrami spectrum and spatial geodesic clustering degree is proposed and the LS-Hotelling T^2 control chart is constructed to achieve curved surface monitoring. The proposed monitoring approach takes full advantage of the geometrical shape and spatial distribution information of non-Euclidean curved surfaces.

The remainder of this paper is organized as follows. "Brief introduction of Laplace–Beltrami spectrum" section introduces the basic idea of Laplace–Beltrami spectrum. "The proposed approach" section describes the detail of the proposed approach. "Numerical simulation" and "Case studies" sections demonstrate the feasibility and application of the proposed approach through numerical simulation and two real-world engineering surfaces case studies. Finally, "Conclusions" section presents conclusions and discusses implications for future research.

Brief introduction of Laplace–Beltrami spectrum

Laplace–Beltrami (LB) operator is defined as the divergence of the gradient, which is the extension of Laplacian operator (Zhao & Castillo, 2022). Different from Laplacian operator deriving from flat space, LB operator is defined on curved space or manifold. In the field of differential geometry, the curved surface is instance of a 2-dimensional manifold. The LB operator encodes the curvature of the manifold, which is usually used to characterize the shape of the curved space or manifold. The definition of LB operator is:

$$\begin{aligned}\Delta_M f &= -\mathrm{div}_M \nabla_M f \\ &= -\frac{1}{\sqrt{\det(\mathbf{g})}} \sum_{j=1}^{k} \frac{\partial}{\partial x^j}\left(\sqrt{\det(\mathbf{g})} \sum_{i=1}^{k} g^{ij} \frac{\partial f}{\partial x^i}\right)\end{aligned} \tag{1}$$

where M denotes a curved surface or 2-manifold, div_M and ∇_M represent the divergence and the gradient of M respectively. f is a function of each point on M, which is given by $f(x^1, x^2, \ldots, x^k) \in C^2$. x^i denotes manifold coordinate and k denotes the number of dimensions of the manifold ($k = 2$ for surfaces). $\mathbf{g}$ is a metric tensor defined by the ambient space on M, $\det(\mathbf{g})$ is the determinant of $\mathbf{g}$, which is computed by a parametric surface $\mathbf{p}(u, v) = (x(u, v), y(u, v), z(u, v))' \,|\, (u, v) \in D \subset \mathbb{R}^2$.

Here, $g^{ij} \in \mathbf{g}^{-1}$ and the definition of $\mathbf{g}$ is:

$$\begin{aligned}\mathbf{g} = \begin{pmatrix} g_{11} & g_{12} \\ g_{12} & g_{22} \end{pmatrix} \Bigg| \; & g_{11} = \langle \mathbf{p}_u, \mathbf{p}_u \rangle, \; g_{12} \\ & = \langle \mathbf{p}_u, \mathbf{p}_v \rangle, \; g_{22} = \langle \mathbf{p}_v, \mathbf{p}_v \rangle\end{aligned} \tag{2}$$

$$\mathbf{p}_u = \frac{\partial \mathbf{p}(u, v)}{\partial u} = \left(\frac{\partial x(u, v)}{\partial u}, \frac{\partial y(u, v)}{\partial u}, \frac{\partial x(u, v)}{\partial u}\right)' \tag{3}$$

$$\mathbf{p}_v = \frac{\partial \mathbf{p}(u, v)}{\partial v} = \left(\frac{\partial x(u, v)}{\partial v}, \frac{\partial y(u, v)}{\partial v}, \frac{\partial x(u, v)}{\partial v}\right)' \tag{4}$$

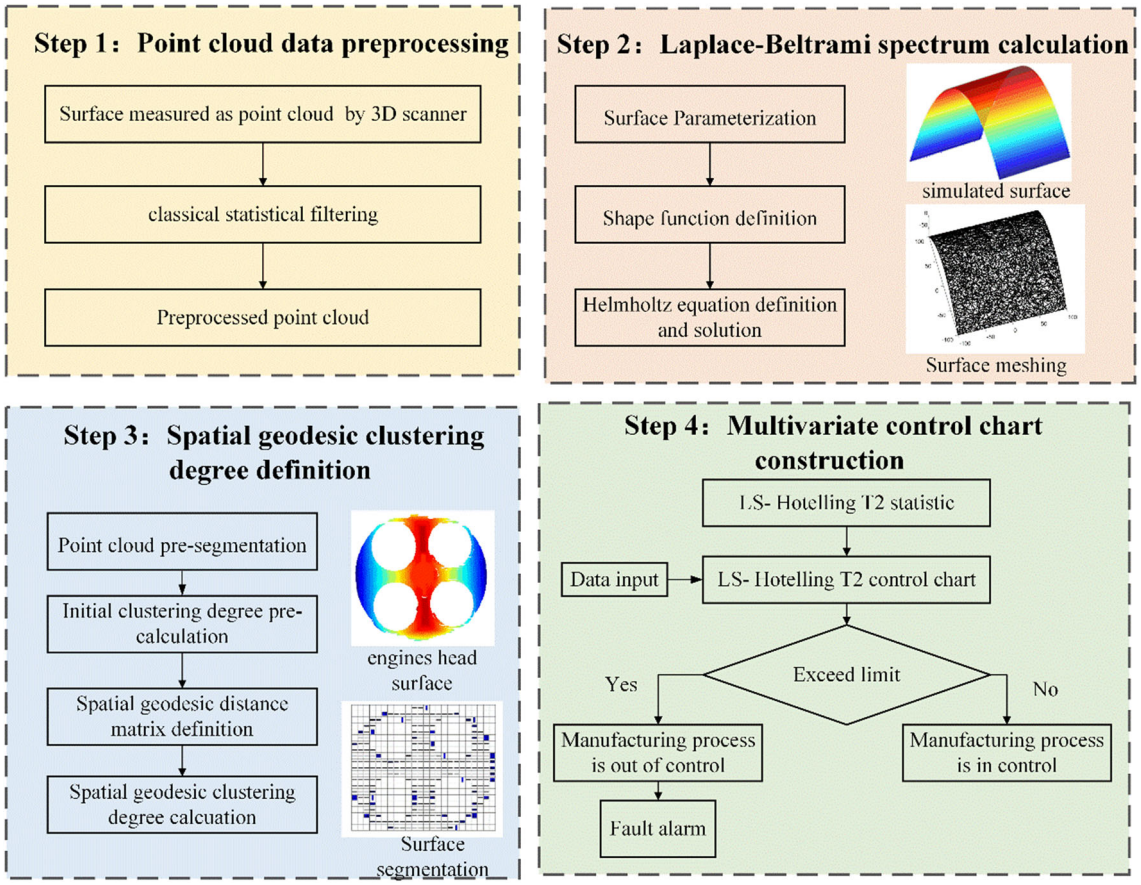

Fig. 1 The framework of the proposed approach

where $\mathbf{p}_u$ and $\mathbf{p}_v$ are the surface different vectors at $\mathbf{p}(u, v)$, $u = x^1$ and $v = x^2$ are local coordinates, and $\langle , \rangle$ represents the standard inner product. Benefitting from the intrinsic geometrical properties and invariant to the curved surface rigid transformation (rotations and translations) of the metric tensor $\mathbf{g}$, the geometrical shape feature of the curved surface M represented by scanned point cloud data can be characterized by the intrinsic differential operator $\mathbf{g}$, which avoids time-consuming registration problems.

Similar to LB operator, the LB operator spectrum also encodes the inherent geometric and topological information in the curved surface or manifold M, which is induced by solving a Laplacian eigenvalue problem:

$$\Delta_M f = \lambda f \tag{5}$$

where f is called eigenfunction and λ is called eigenvalue, and this formula is also known as the Helmholtz partial differential equation. The solution $\{\lambda_i\}_{i=0}^{\infty}(0 = \lambda_1 \leq \lambda_2 \leq \lambda_3 \ldots \leq \lambda_i)$ of the Helmholtz's equation is the set of eigenvalues, which is named LB spectrum. The slope of LB spectrum $\lim_{i\to\infty} \frac{\lambda_i}{i} = \frac{4\pi}{Vol(M)}$ is related to the volume of the manifold, which indicates the shape difference between curved surfaces. More importantly, LB operator spectrum can reflect the variations of the manifold in a continuous form, which can be considered as a powerful tool for shape identification and monitoring the small geometrical changes of the curved surface.

The proposed approach

Overview of the proposed approach

This section describes an overview of the proposed curved surface monitoring approach based on geometrical-spatial joint features using point cloud data. It consists of point cloud data preprocessing, Laplace–Beltrami spectrum calculation, spatial geodesic clustering degree definition, and multivariate control chart construction. The framework of the developed monitoring approach is shown in Fig. 1, and the procedure involves the following steps.

Step 1 *Point cloud data preprocessing* Read the point cloud data of measured curved surface and eliminate outliers, noisy and redundant points.

Step 2 *Laplace–Beltrami spectrum calculation* Convert the point cloud data into triangular mesh and achieve the Laplace–Beltrami operator discretization. Define the shape function on each triangular mesh nodal point and translate the Helmholtz equation into a characteristic equation by the Galerkin variational formula. Then, the Laplace–Beltrami spectrum is obtained by calculating the partial derivative of the shape functions and solving the characteristic equation.

Step 3 *Spatial geodesic clustering degree definition* A Spatial Geodesic Distance Matrix is defined to find out the optimal segmenting size of the point cloud data with the largest spatial correlation. The spatial geodesic clustering degree of the point cloud data is determined in the optimal segmenting size.

Step 4 *Multivariate control chart construction* A novel multivariate statistic is generated by LB spectrum and spatial aggregation. The Hotelling's T^2 control chart is constructed to achieve the curved surface monitoring.

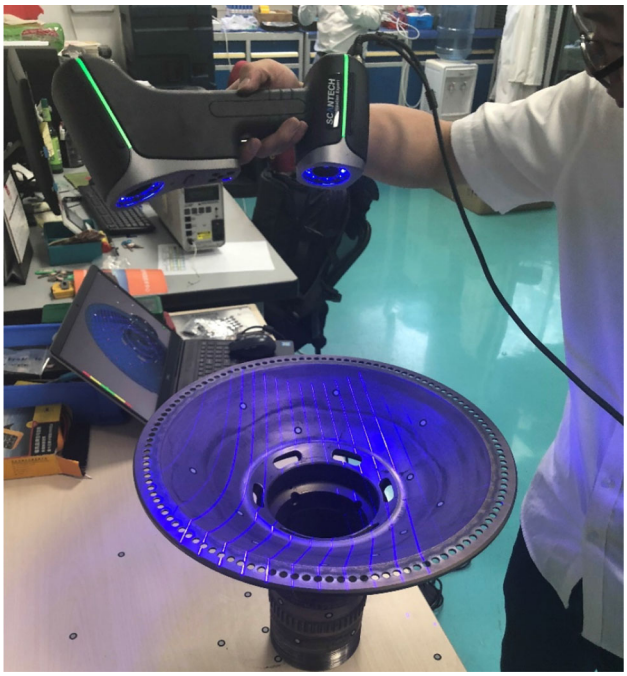

Fig. 2 KSCAN-magic

Point cloud data preprocessing

Engineering curved surfaces are measured by a 3D laser scanning instrument, and massive and high-density point cloud data are generated to characterize each curved surface. The 3D laser scanner used in this paper is called KSCAN-Magic, which is a composite 3D scanner of infrared and blue laser, as it shown in Fig. 2. It can emit laser spots or linear lasers to the measured object, and obtain the 3D laser point cloud data of the object quickly, accurately and efficiently. KSCAN-Magic has a variety of working modes including: blue cross laser high-speed scanning, infrared parallel laser large-format scanning, blue parallel laser fine scanning, single blue laser deep hole scanning, and built-in global photogrammetry system. The scanning area can reach 1440 mm × 860 mm, the accuracy is 0.02 mm, the volume accuracy is 0.030 mm/m, and the depth of field is 925 mm. The reference distance is 300 mm, the single point repeatability is 0.030 mm, the tracking frequency is 60 Hz, and the boundary accuracy is 0.030 mm. In the blue parallel laser fine scanning mode, there are 41 laser lines and the scanning speed of 1,350,000 times per second, the entire complex surface data can be accurately acquired with millions of points. Based on the application requirements of different fields, multiple measurement modes can be freely switched. It can output a variety of three-dimensional point cloud data to represent the measured entire surface, and has a strong ability to adapt to different harsh work environments. The advantages of KSCAN-Magic contain large measurement distance, anti-interference, large density of measurement points, high accuracy and strong robustness. Generally, it is only affected by the self-accuracy, the light intensity of the laser beam and the surface characteristics of the measured object, which is not easily affected by external light or random operation error. The measured rotor curved surface and measured cylinder head surface are shown in Fig. 3. Due to the reasons of surface structure, roughness, texture characteristics and the measurement environment, the raw measured point cloud data exists a number of isolated noisy points, obvious outliers and redundant points, which have a large impact on the geometrical shape and spatial distribution of the curved surface. Therefore, it is necessary to eliminate these obvious wrong points without changing the intrinsic properties of the curved surface and preserve feature details such as textures and edges. The classical filter assumes that the distance between each point and its neighboring points in a point cloud data obeys a certain statistical distribution, which is obtained by calculating the distance between each point and its k neighboring points. Due to external disturbances, error points usually occur far away from other dense point cloud regions, which leads to the distribution of error points largely failing to conform to this statistical distribution. Therefore, the error points should be removed.

The classical statistical filtering is adopted to achieve the point cloud data denoising process, which consists of three steps including nearest neighbor average distance calculation, distance threshold definition and wrong points removing. The specific denoising process is as follows: First, calculate the distance $d_i|i = 1, 2, \ldots k$ from point $p_1(x_1,$

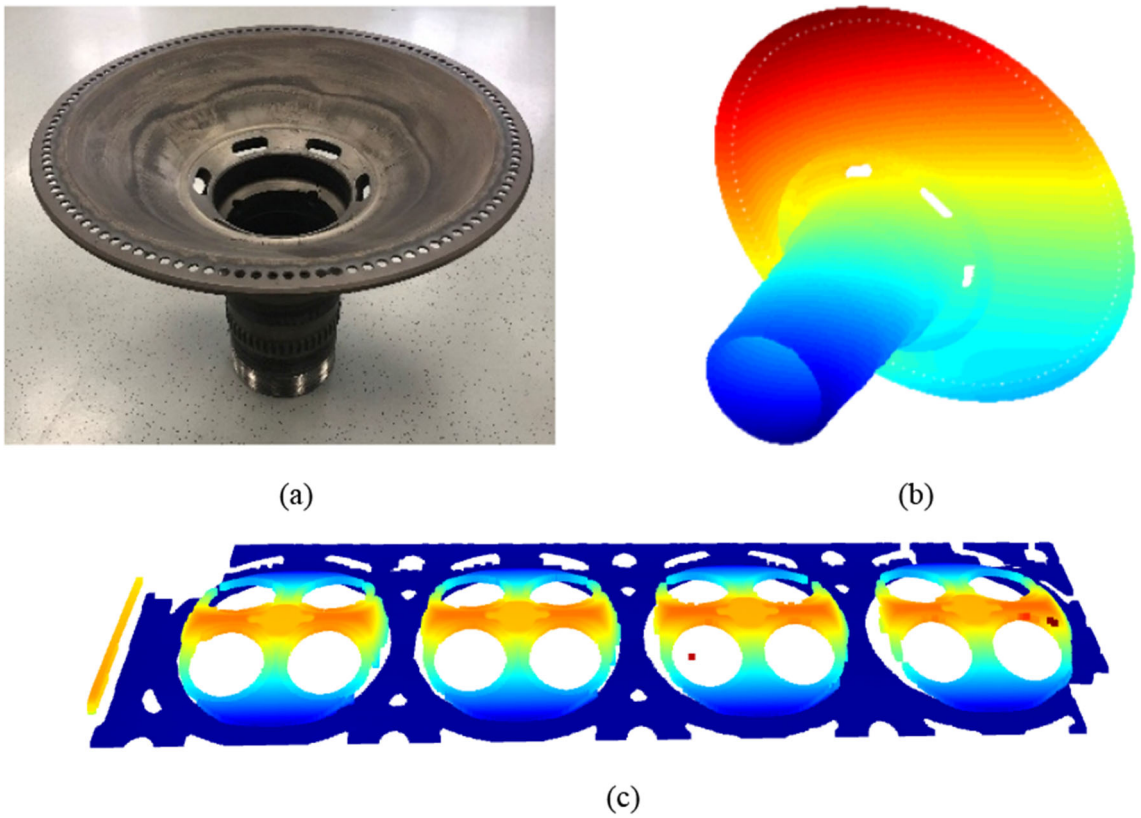

Fig. 3 **a** Rotor, **b** Measured rotor surface, **c** Measured cylinder head

Fig. 4 **a** Initial point cloud Q_0, **b** Preprocessed point cloud Q

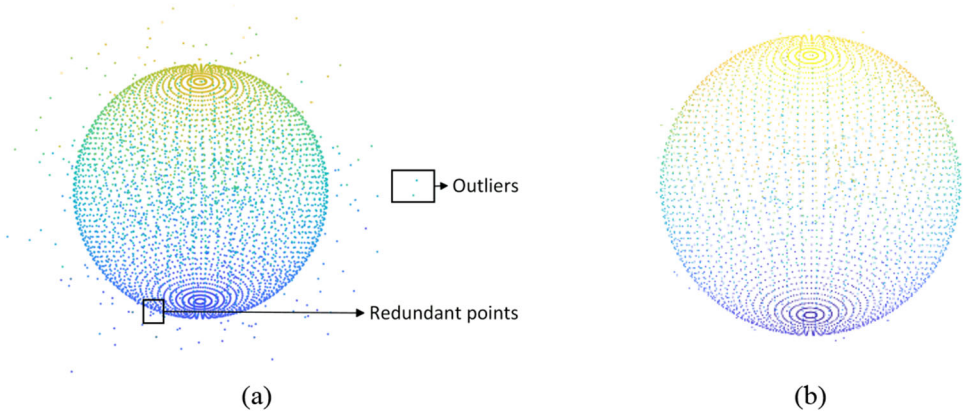

y_1, z_1) to its k neighboring points. Assume the average of d_1, $d_2 \ldots d_k$ is d, then these distances obey the Gaussian distribution $f(d)$ with a mean of μ_d and a variance of σ_d, where $d = \frac{1}{k}\sum_{l=1}^{k}\sqrt{(x-x_1)^2+(y-y_1)^2+(z-z_1)^2}$ and $f(d) = \frac{1}{\sigma_d\sqrt{2\pi}}e^{-\frac{(d-\mu_d)^2}{2\sigma_d^2}}$. Then recalculate the distance d_i' $|i = 1, 2, \ldots k$ from point $p_1(x_1, y_1, z_1)$ to its k neighboring points, k is generally defaulted to 4. When it satisfies $d_i \in (\mu_d - 3\sigma_d, \mu_d + 3\sigma_d)$, reserve the point, otherwise eliminate it. Finally repeat the above operations for all points in the point cloud data, the preprocessed point cloud data can be obtained. As for a measured curved surface M represented by the initial point cloud Q_0, an example of point cloud data denoising is shown in Fig. 4, and Q is the preprocessed point cloud.

Laplace–Beltrami spectrum calculation

Benefitting from the superiority of LB spectrum intrinsic property, it is independent of the ambient space coordinates of the embedded object, thereby being widely used to describe the geometry of workpieces. Moreover, the LB

spectrum can be compared between workpieces without pre-registration and localization, totally indicating the shape change of continuous machining workpieces in the production line. Therefore, it can be considered as a geometric shape indicator for the curved surface monitoring, such as the blade profile deformation, the cylinder head combustion chamber volume and aircraft cabin surface variation.

In order to obtain the accurate LB spectrum, it has already appeared many calculation approaches including localized mesh Laplacian approximation, FEM approximation and so on. The localized mesh Laplacian approximation derives from the theory of heat diffusion and wave propagation in Physics (Zhao & Castillo, 2021), which is only suitable for closed surfaces without boundaries. In contrast, the advantage of FEM approximation is that not only can be applied to open surfaces or volumetric data, but also can handle the boundary conditions. Hence, one of the FEM approximation approaches called Galerkin variational formula is adopted to calculate LB spectrum by solving Helmholtz equation in this paper. The detailed procedures are explained as follows.

Step 1: Surface parameterization

It is necessary to discretize surface when solving the LB spectrum, for a two-dimensional manifold on a three-dimensional surface, which is represented by $\mathbf{p}(u, v) = (x(u, v), y(u, v), z(u, v))' \big| (u, v) \in D \subset \mathbb{R}^2$.

Step 2: Shape function definition

The shape function is mainly aim at each triangle point of the triangular mesh data. convert the curved surface M of point cloud data into triangular mesh data. Generally, the shape functions $h_{l(u,v)}$ are usually characterized by algebraic polynomial approximations such as:

$$h_l(u, v) = c_{l,1} + c_{l,2}u + c_{l,3}v \tag{6}$$

where l represents the nodes in triangles, and $c_{l,i}$ represents the coefficients, u and v denote local coordinates respectively. $h_l(u, v)$ is linear shape function which derives from three vertices of a triangle. There are many kinds of shape equations, the linear shape function is the simplest and fast approach. With the requirements of the production takt and real-time monitoring, the linear shape function is used in this paper. The specific solution steps are as follows:

Condition 1: Considering the triangular mesh data only contains one triangle, and the initial coordinates of three nodes of the triangle are $P_1(0, 0, 0)$, $P_2(0, 1, 0)$, $P_3(1, 0, 0)$. The triangle can be expressed parametrically as $\mathbf{p}(u, v) = (u, v, 0)$ with $0 \le u \le 1, 0 \le v \le 1, u + v \le 1$ and the initial coordinates can be transformed into three nodes $P_1 = \mathbf{p}(0, 0)$, $P_2 = \mathbf{p}(0, 1)$, $P_3 = \mathbf{p}(1, 0)$, the initial metric tensor $\mathbf{g}_0$ can be obtained by:

$$\begin{aligned}\mathbf{g}_0 &= \begin{pmatrix} g_{11} & g_{12} \\ g_{12} & g_{22} \end{pmatrix} = \begin{pmatrix} \frac{\partial \mathbf{p}(u,v)}{\partial u} \cdot \frac{\partial \mathbf{p}(u,v)}{\partial u} & \frac{\partial \mathbf{p}(u,v)}{\partial u} \cdot \frac{\partial \mathbf{p}(u,v)}{\partial v} \\ \frac{\partial \mathbf{p}(u,v)}{\partial u} \cdot \frac{\partial \mathbf{p}(u,v)}{\partial v} & \frac{\partial \mathbf{p}(u,v)}{\partial v} \cdot \frac{\partial \mathbf{p}(u,v)}{\partial v} \end{pmatrix} \\ &= \begin{pmatrix} 1 & 0 \\ 0 & 1 \end{pmatrix} = I \end{aligned} \tag{7}$$

where $\frac{\partial \mathbf{p}(u,v)}{\partial u} = (1, 0, 0)$ and $\frac{\partial \mathbf{p}(u,v)}{\partial v} = (0, 1, 0)$. Subsequently, as for the first node $P_1 = \mathbf{p}(0, 0)$ of the triangle, the shape function $h_1(u, v)$ can be solved in the following equations:

$$\begin{aligned} &h_1(u, v) = c_{1,1} + c_{1,2}u + c_{1,3}v | h_1(P_1) = 1, \\ &h_1(P_2) = 0, h_1(P_3) = 0 \end{aligned} \tag{8}$$

and it can obtain $c_{1,1} = 1$, $c_{1,2} = -1$, $c_{1,3} = -1$ and $h_1(u, v) = 1 - u - v$. It is noted that the shape function of k th node of the triangle satisfies $h_l(P_k) = 1(l = k)$ and $h_l(P_k) = 0$ $(l \ne k)$.

Condition 2: Considering triangular mesh data with $r(r > 1)$ triangles, for the coordinates of three nodes of a random triangle $P_1(x_1, y_1, z_1)$, $P_2(x_2, y_2, z_2)$, $P_3(x_3, y_3, z_3)$, it can be converted into Condition 1 ($P_k = \mathbf{p}(u, v) = (u, v, 0)$ $|k = 1, 2, 3)$ through the curved surface parameterization:

$$\begin{aligned} p(u, v) = (&x_1 + u(x_3 - x_1) + v(x_2 - x_1), \\ &y_1 + u(y_3 - y_1) + v(y_2 - y_1), \\ &z_1 + u(z_3 - z_1) + v(z_2 - z_1)) \end{aligned} \tag{9}$$

and it still satisfy $P_1 = \mathbf{p}(0, 0)$, $P_2 = \mathbf{p}(0, 1)$, $P_3 = \mathbf{p}(1, 0)$. Conversely, the metric tensor $\mathbf{g}$ is recalculated for the parameterization:

$$\mathbf{g} = \begin{pmatrix} \|\mathbf{p}_3 - \mathbf{p}_1\|^2 & (\mathbf{p}_3 - \mathbf{p}_1) \cdot (\mathbf{p}_2 - \mathbf{p}_1) \\ (\mathbf{p}_3 - \mathbf{p}_1) \cdot (\mathbf{p}_2 - \mathbf{p}_1) & \|\mathbf{p}_3 - \mathbf{p}_1\|^2 \end{pmatrix} \tag{10}$$

where $\frac{\partial \mathbf{p}(u,v)}{\partial u} = (x_3 - x_1, y_3 - y_1, z_3 - z_1)$ and $\frac{\partial \mathbf{p}(u,v)}{\partial v} = (x_2 - x_1, y_2 - y_1, z_2 - z_1)$. And The metric tensor $\mathbf{g}$ is the most important parameter in solving the LB spectrum.

Step 3: Helmholtz equation definition and solution

It is necessary to perform variable separation on the LB operator when solving the LB spectrum, thereby leading to an eigenproblem called Helmholtz equation. A classical FEM approximation approach named Galerkin variational formula is used to find the function f defined on the curved surface M, which satisfies the following equation:

$$-\int_M \nabla f \cdot \nabla \phi dV = \lambda \int_M \phi f dV \tag{11}$$

where $\left\{ f^N = \sum_{m=1}^{N} u_m h_m | f \in V \right\}$ is a characteristic function consists of several eigenfunctions h_m, u_m is the coefficient and λ is eigenvalue. V and N are respectively the function space and the number of eigenfunctions. $\nabla\phi \cdot \nabla f$ is named the first differential parameter of Beltrami, which is defined as:

$$\nabla\phi \cdot \nabla f = \partial\phi' \mathbf{g}^{-1} \partial f = \sum\nolimits_{i,j} g^{ij} \partial_i \phi \partial_j f \tag{12}$$

then, the Eq. (11) can be transformed into N equations:

$$\begin{aligned} &-\int_M \sum g^{ij} \partial_i h_j \partial_j \left(\sum\nolimits_{m=1}^{N} u_m h_m \right) dV = \lambda \int_M h_l \left(\sum\nolimits_{m=1}^{N} u_m h_m \right) dV,\ l = 1, 2, \ldots N \\ &\sum\nolimits_{m=1}^{N} u_m \left(-\int_M \sum g^{ij} \partial_i h_j \partial_j h_m dV \right) = \lambda \sum\nolimits_{m=1}^{N} u_m \left(\int_M h_l h_m dV \right),\ l = 1, 2, \ldots N \end{aligned} \tag{13}$$

and the N equations can be translated as a generalized eigenvalue problem in the form of a matrix:

$$\mathbf{AU} = \lambda \mathbf{BU} \tag{14}$$

Equation (14) is called characteristic equation, where $\mathbf{U} = \{u_i | i = 1, 2, \ldots, n\}$ denotes the set of coefficients, $\mathbf{A}$ and $\mathbf{B}$ both are Gram matrices which satisfy:

$$\mathbf{A}_{lm} = -\langle \nabla h_l, \nabla h_m \rangle = -\sum\nolimits_{i,j} g^{ij} \int_M \partial_i h_l \partial_j h_m dV \tag{15}$$

$$\mathbf{B}_{lm} = \langle h_l, h_m \rangle \tag{16}$$

Due to $dV = \sqrt{\det(\mathbf{g})} du dv$. By virtue of this, the analytical expression of matrices $\mathbf{A}$ and $\mathbf{B}$ are changed as follows:

$$\mathbf{A}_{lm} = -\int_M \sum g^{ij} \partial_i h_j \partial_j h_m \sqrt{\det(\mathbf{g})} du dv \tag{17}$$

$$\mathbf{B}_{lm} = \sqrt{\det(\mathbf{g})} \int_M h_l h_m du dv \tag{18}$$

where l and m denote the indexes of the (l, m)th element in matrices $\mathbf{A}$ and $\mathbf{B}$. It is worth noting that the matrices $\mathbf{A}$ and $\mathbf{B}$ both are sparse and symmetric, which ensure LB spectrum is real spectrum. At the same time, the LB spectrum estimation is high-efficiency and accurate based on the matrix sparsity. Finally, the LB spectrum $\{\lambda_i\}_{i=0}^{\infty}$ is obtained.

Spatial geodesic clustering degree definition

Spatial geodesic clustering degree is a significant index to characterize the distribution of points within the point cloud data. Current researches mainly focus on efficient extraction approaches of the feature structure of point cloud data, and little attention is paid to the distribution of the point cloud itself. The previous approaches of representing the point cloud data distribution are generally to divide the point cloud data into a number of standardized blocks. Then the number of points falling within each block is calculated respectively, and the point cloud data distribution is described by the further statistical operations including arithmetic mean value and weighted mean value of point in these blocks. Likewise, the distance between points in the point cloud data is also directly used as the distribution metric. The above approaches cannot reflect the distribution of point clouds well and sensitively. Therefore, it is crucial to obtain representative feature parameters which can reveal the real distribution information of the point cloud data in curved surface monitoring. A new feature parameter called spatial geodesic clustering degree (SDCD) is defined in this paper, which is based on the proposed spatial geodesic distance matrix. The SDCD adopts the geodesic distance between points, and fully reflects the spatial correlation of the point cloud. The definition process of SDCD is summarized as:

Step 1: Point cloud pre-segmentation

Due to the numerous the large number and uneven distribution of curved surface point clouds, it is essential to implement point cloud pre-segmentation. As for the measured curved surface M, it is represented by the point cloud Q. The determination of segmentation size should correspond to the dimensions and distribution attributes of the point cloud. Choosing a larger segmentation size would yield point cloud data with reduced detailing, while selecting a smaller segmentation size could lead to blocks containing only a few points. As a result, it is essential to pinpoint the optimal block size within a suitable range. Set B as the segmenting interval, $W \times H$ as the initial segmenting size, n as the number of segmented point cloud block, and then the point cloud Q can be divided into a series of segmented point cloud block Q_n, and the size of Q_n satisfies:

$$Q_n = WQ_n \times HQ_n = [W + (n-1) \times B] \times [H + (n-1) \times B] \tag{19}$$

where $WQ_n \times HQ_n$ denotes the segmenting size of the nth segmented point cloud.

Step 2: Initial clustering degree pre-calculation

The various segmenting sizes have a great impact on the distribution description of the point cloud Q. In order to

determine the optimal segmenting size, the initial clustering degree ds_n of each segmented point cloud block Q_n is calculated firstly.

$$ds_n = \frac{\sum_{i=1}^{\lfloor WQ/WQ_n \rfloor} \sum_{j=1}^{\lfloor HQ/HQ_n \rfloor} V_{ij}^2}{N_T \sqrt[4]{B_d / B_t}} \tag{20}$$

where WQ and HQ denote the size of the point cloud Q, N_T is the number of the point cloud Q. B_d denotes the sum of the number of segmented point cloud blocks which exist points in them, B_t denotes the total number of blocks, V_{ij} denotes the number of points of each segmented point cloud block Q_n, i and j denote the indices of blocks.

Step 3: Spatial geodesic distance matrix definition

Spatial correlation describes the relationship between the point and the neighbor point in the same space region, which is an important property in spatial statistics. Greary's C index is one of the spatial autocorrelation coefficients, the distribution range of its value is [0,2], and the mathematical expectation is 1, which is used to distinguish the degree of spatial autocorrelation. As for the segmented point cloud block Q_n, the Greary's C index C_n is calculated as:

$$C_n = (r-1)\frac{\sum_{i=1}^{r}\sum_{j=1}^{r} w_{ij}(ds_{ni} - ds_{nj})}{2rS^2 \sum_{i=1}^{r}\sum_{j=1}^{r} w_{ij}} \tag{21}$$

$$r = \lfloor WQ/WQ_n \rfloor \times \lfloor HQ/HQ_n \rfloor \tag{22}$$

$$S^2 = \sum_{i=1}^{r} (ds_{ni} - \overline{ds})^2 \Big/ r \tag{23}$$

where r denotes the number of the segmented point cloud block Q_n, ds_{ni} and ds_{nj} denote of the spatial geodesic clustering degree the ith and jth segmented point cloud block Q_{ni} and Q_{nj}, ds denotes the spatial geodesic clustering degree of the point cloud Q, and w_{ij} denotes the element of the spatial distance matrix. There are different distance matrices such as spatial adjacency matrix, spatial geographical distance matrix and spatial economic distance matrix, which have directly influence on the accuracy of Greary's C index. since the curved surface belongs to the three-dimensional point cloud, and it has curvature discontinuity, thereby the traditional two-dimensional spatial distance matrices are not suitable for the curved surface, which cannot reflect the three-dimensional feature information. Therefore, a new spatial distance matrix named spatial geodesic distance matrix **GW** is proposed, which can describe the distribution of the curved surface point cloud.

$$\mathbf{GW}(i, j) = \min_{1 \le k \le n} (d(i, k) + d(k, j)) \tag{24}$$

The element gw_{ij} of spatial geodesic distance matrix **GW** represents the geodesic distance between the center of gravity of segmented point cloud block Q_{ni} and Q_{nj}. The spatial geodesic distance matrix **GW** reflects the specific positional relationship between point cloud blocks and blocks, which clarify further point cloud spatial correlation. Then the Greary's C index C_n^g is recalculated as:

$$C_n^g = (r-1)\frac{\sum_{i=1}^{r}\sum_{j=1}^{r} gw_{ij}(ds_{ni} - ds_{nj})}{2rS^2 \sum_{i=1}^{r}\sum_{j=1}^{r} gw_{ij}} \tag{25}$$

Step 4: Spatial geodesic clustering degree

According to the segmented point cloud block Q_n, it is essential to determine the optimal segmenting size $WQ_k \times HQ_k$ and the optimal number of segmented point cloud block k. The spatial geodesic clustering degree computed with the optimal segmenting size is defined as spatial geodesic clustering degree dsg:

$$dsg = \frac{\sum_{i=1}^{\lfloor WQ/WQ_k \rfloor} \sum_{j=1}^{\lfloor HQ/HQ_k \rfloor} V_{ij}^2}{N_T \sqrt[4]{B_d / B_t}} \tag{26}$$

The number of the curved surface point cloud is large enough, and it obeys normal distribution approximately in statistics. With the assumption of a normal distribution, Z test is adopted to implement significance test for Greary's C index C_n^g:

$$Z(C_n^g) = \frac{C_n^g - 1}{\sqrt{Var[C_n^g]}} \tag{27}$$

where it satisfies $Var[C_n^g] = \left(\frac{(2S_1+S_2)(r-1)-4S_0^2}{2(r+1)S_0^2}\right)$, $S_0 = \sum_{i=1}^{r}\sum_{j=1}^{r} gw_{ij}$, $S_1 = \frac{1}{2}\sum_{i=1}^{r}\sum_{j=1}^{r}(gw_{ij} + gw_{ji})^2$, $S_2 = \sum_{i=1}^{r}\left(\sum_{j=1}^{r} gw_{ij} + \sum_{j=1}^{r} gw_{ji}\right)^2$.

At the significance level of 5%, if $Z(C_n^g) > 1.96$, then show that the Greary's C index is significant and the spatial units within the study area attribute values are spatially significantly correlated. Therefore, the spatial autocorrelation degree of the attribute values can be judged based on the magnitude of the Greary's C index and then the optimal segmenting size of spatial autocorrelation can be found.

Multivariate control chart construction

Multivariate control chart is a powerful tool for monitoring small drifts in multivariate systems including chemical process, semiconductor manufacturing and high-end manufacturing equipment with complex curved surfaces, which is a multivariate extension and promotion of univariate control chart. In fact, the multivariate control chart is not a simple superposition of univariate control charts, but a statistical management approach to control multiple quality parameters at the same time, thereby monitoring the tested sample from a variety of dimensions and reflecting the product manufacturing process anomalies. Phase II of the control chart is mainly designed for manufacturing process monitoring, which is the focus in this paper.

Hotelling T^2 control chart is the most familiar and widely used multivariate process-monitoring and control procedure, which is adopted to monitor the mean vector of the process. It is a directionally invariant control chart to detect a shift in the mean vector depends only on the magnitude of the shift, not the direction of the shift. Specifically, the statistic T^2 represents the square of the distance in the statistical sense for the combination of different multivariate observations. Suppose that it has t variances given by $\mathbf{x} = [x_1, x_2, \ldots, x_t]$, which obeys the multivariate normal distribution. After the test, m groups of sample data are obtained, and each group has n test values. Then the sample mean vector $\bar{\mathbf{x}}_k$ and the mean vector of each quality characteristic $\bar{\mathbf{x}}_j$ can be calculated as:

$$\begin{aligned} \bar{\mathbf{x}}_k &= \left\{\bar{x}_{jk} | j = 1, 2, \ldots, t\right\} = [\bar{x}_{1k}, \bar{x}_{2k}, \ldots, \bar{x}_{tk}] \\ \bar{\mathbf{x}}_j &= \left\{\bar{\bar{x}}_j | j = 1, 2, \ldots, t\right\} = \left[\bar{\bar{x}}_1, \bar{\bar{x}}_2, \ldots, \bar{\bar{x}}_t\right] \end{aligned} \tag{28}$$

where $\bar{x}_{jk} = \frac{1}{n}\sum_{i=1}^{n} x_{ijk}$, $\bar{\bar{x}}_j = \frac{1}{m}\sum_{k=1}^{m} \bar{x}_{jk}$, $i = 1, 2, \ldots, n$, $k = 1, 2, \ldots, m$, and x_{ijk} denotes the ith observation on the jth quality characteristic in the kth sample. Let $\mathbf{X} = \bar{\mathbf{x}}_k$ and $\boldsymbol{\mu} = \bar{\mathbf{x}}_j$, the statistic T^2 is defined as:

$$\mathbf{T}^2 = n(\mathbf{X} - \boldsymbol{\mu})^T \sum^{-1} (\mathbf{X} - \boldsymbol{\mu}) \tag{29}$$

where $\sum^{-1}$ denotes the covariance matrix. Subsequently, the control limits for T^2 control chart in stationary state can be given as follows:

$$\begin{aligned} \mathrm{UCL} &= \frac{t(m-1)(n-1)}{mn - m - t + 1} F_{\alpha, t, mn-m-t+1} \\ \mathrm{LCL} &= 0 \end{aligned} \tag{30}$$

In some industrial applications, the subgroup size of the sample satisfies $n = 1$, which occurs frequently in chemical process, structured surfaces and complex curved surfaces. By virtue of this, a joint control chart called LS-Hotelling T^2 is proposed to achieve curved surface monitoring. The joint statistic LS-T^2 consists of Laplace–Beltrami spectrum and spatial geodesic clustering degree, which is defined as:

$$\mathbf{T}_{LS}^2 = (\mathbf{LSX} - \boldsymbol{\mu})^T \sum^{-1} (\mathbf{LSX} - \boldsymbol{\mu}) \tag{31}$$

where $\mathbf{LSX} = \left[\boldsymbol{\lambda}, \mathbf{dsg}\right]$ is the bivariate statistic. $\boldsymbol{\lambda}$ is the set of Laplace–Beltrami spectrum, which is used to represent the evolution of curved surface shape. **dsg** is the set of spatial geodesic clustering degree, which reveals the variation rules of the distribution of points within the curved surface. The two variables are statistically independent normally distributed, thereby indicating the existence state of the curved surface from different dimensions. The corresponding control limits for LS-Hotelling T^2 control chart in stationary state can be given as follows:

$$\begin{aligned} \mathrm{UCL} &= \frac{(m-1)^2}{m} \beta_{\alpha, t/2, (m-t-1)/2} \\ \mathrm{LCL} &= 0 \end{aligned} \tag{32}$$

where $\beta_{\alpha, p, q}$ and $F_{\alpha, p, q}$ denote β-distribution and F-distribution at significance level α with parameters p and q. Comparing with the univariate control chart, the proposed LS-Hotelling T^2 control chart can monitor the curved surface from two aspects including the change of the shape and the distribution of the points, which has a strong sensitivity to the drifts of the curved surface and captures anomalies of the process state more quickly.

Numerical simulation

Curved surface simulation

Due to the variable Gaussian curvature, the complex curved surfaces have various shapes without symmetry or rotational translation, and cannot be expressed parametrically. Meantime, the curved surface profile quality is closely related to the qualification of the workpieces, but it usually exists various defects such as scratches, holes and grooves when the manufacturing process is out-of-control. Hence, it is an urgent problem to monitor the curved surface profile, thereby reflecting the stability of the manufacturing process. In order to validate the effectiveness of the proposed curved surface monitoring approach, a series of curved surfaces are generated by the function:

$$M_{0(x,y)} = \eta * y^2 | x \in [-200, 200],\ y \in [-200, 200] \tag{33}$$

where η denotes a parameter to determine the curvature of curved surfaces. In this paper, forty curved surfaces $M_i | i = 1, 2, \ldots, 40$ of size 200 mm × 200 mm are simulated, and

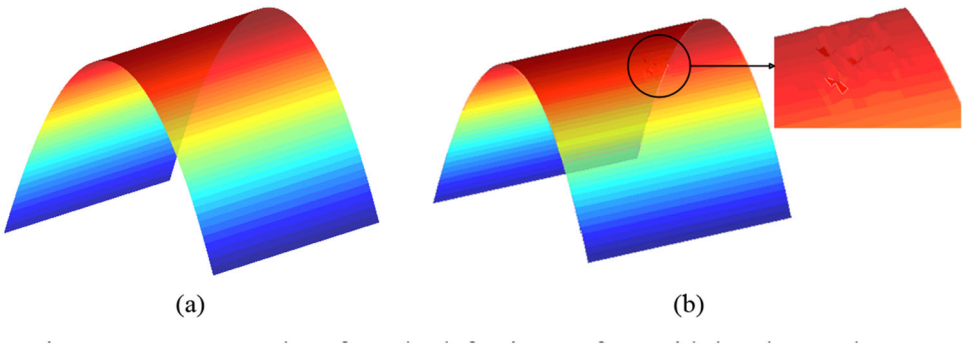

Fig. 5 **a** A normal surface, **b** A defective surface with local scratches

they are assumed to be manufactured in a steady production process. The surfaces $M_i|i = 36, 37, \ldots, 40$ are simulated as out-of-control surfaces with small defects. As an example, a normal surface and a defective surface with local scratches are simulated in Fig. 5 respectively.

Since there are no large number of noisy points, obvious outliers and redundant points on the these simulated curved surfaces, and the point cloud preprocess is unnecessary in the simulation experiment. Firstly, the LB spectrum of these forty surfaces are calculated respectively. During the LB spectrum calculation, the shape function at each triangle point of the triangular mesh data of the curved surface is obtained as the algebraic polynomial approximation $h_l(u, v) = h_l^1(u, v) = c_{l,1} + c_{l,2}u + c_{l,3}v$. The characteristic equation is obtained by substituting the shape function $h_l(u, v)$, and the matrices **A** and **B** are solved by the partial derivative of the shape function. The set of eigenvalues $\{\lambda_i|i = 1, 2, \ldots, 40\}$ in the characteristic equation can be obtained, namely the LB spectrum of the curved surface. Since each point in the triangular mesh data can obtain an LB spectrum value, and the first fifty eigenvalues are relatively stable (Zhao & Castillo 2022). When the LB spectrum is calculated, the first fifty spectrum values demonstrate a consistent upward trend (Zhao & Castillo 2022), and each point cloud has similar LB spectrum values. Therefore, the average value of the first fifty eigenvalues is adopted as the representative LB spectrum value for the curved surface, and the LB spectrum of the simulated forty curved surfaces are shown in Table 1.

Then, setting the initial segmenting size as $W \times H = 5\text{ mm} \times 5\text{ mm}$, the cutoff segmenting size as $15\text{ mm} \times 15\text{ mm}$, and the segmenting interval $B = 1$ mm. Hence, the simulated forty curved surfaces are segmented as a series of segmented point cloud block $Q_n = WQ_n \times HQ_n = [5 + (n-1) \times 1] \times [5 + (n-1) \times 1]$.

The spatial geodesic distance matrix **GW** is constructed based on the geodesic distance $\mathbf{GW}(i, j)$ and the spatial geodesic clustering degree dsg is calculated for different segmented block sizes. Greary's C index and Z-test are calculated according to different spatial geodesic clustering degree. Figures 6 and 7 show the result of Greary's C index and Z-test for the first simulated curved surface, respectively. Since Greary's C satisfies $C_n \in [0, 2]$, $C_n < 1$ means positive spatial autocorrelation, $C_n > 1$ means negative spatial autocorrelation, $C_n = 1$ means there is no spatial autocorrelation, and $C_n = 0$ or $C_n = 2$ denotes the strongest spatial autocorrelation. According to Greary's C index and $C_n^g Z(C_n^g) > 1.96$, it shows that the Greary's C index is significant and the spatial units which segmented by each size are spatially significantly correlated, and the segmented block size $5\text{ mm} \times 5\text{ mm}$ with the smallest Greary's C index is selected as the optimal block size. Repeat the above procedures for the rest 39 simulated curved surfaces, it finds that the optimal block size is still $5\text{ mm} \times 5\text{ mm}$, that is because the distribution of these curved surfaces is roughly similar and the variations among the curved surfaces belong small shifts. Therefore, all the curved surfaces of $200\text{ mm} \times 200\text{ mm}$ is divide into 1600 pieces with $5\text{ mm} \times 5\text{ mm}$. Table 2 shows the spatial geodesic clustering degree values based on the optimal block size of the simulated forty curved surfaces.

To ensure the normality of the data, the normality of the two variables is assessed using the Anderson–Darling test in this paper. Table 3 shows the normality test results, the Anderson–Darling statistics for two variables do not exceed the critical values and obey normal distribution. The results indicates that the data distribution of the variable aligns statistically well with a normal distribution, which ensuring the validity and applicability of two variables.

Finally, the LB spectrum and spatial geodesic clustering degree of the simulated forty curved surfaces are used to construct the statistic joint multivariate statistic $T_{LSi}^2 = n(\mathbf{LSX}_i - \boldsymbol{\mu}_0)' \sum^{-1} (\mathbf{LSX}_i - \boldsymbol{\mu}_0) | i = 1, 2, \ldots 40$, and $\mathbf{LSX}_i = [\lambda_i, dsg_i]$ is the mass characteristic matrix. Figure 8 shows the monitoring result of the numerical simulation using the proposed LS-Hotelling T^2 control chart, and the control limit UCL = 9.98. It can be seen that the LS-T^2 statistic of the 36th–40th surfaces with defects are significantly out of the control limit, and the control chart issues an alarm in time. Moreover, it demonstrates that the proposed approach can effectively detect the small shifts of curved surface profile during the manufacturing process.

Table 1 LB spectrum of the simulated forty curved surfaces

Sample number	M_1	M_2	M_3	M_4	M_5	M_6	M_7	M_8
LB spectrum	0.0518	0.0491	0.0540	0.0536	0.0473	0.0571	0.0429	0.0539
Sample number	M_9	M_{10}	M_{11}	M_{12}	M_{13}	M_{14}	M_{15}	M_{16}
LB spectrum	0.0576	0.0519	0.0329	0.0579	0.0607	0.0569	0.0475	0.0406
Sample number	M_{17}	M_{18}	M_{19}	M_{20}	M_{21}	M_{22}	M_{23}	M_{24}
LB spectrum	0.0548	0.0494	0.0590	0.0616	0.0521	0.0543	0.0437	0.0402
Sample number	M_{25}	M_{26}	M_{27}	M_{28}	M_{29}	M_{30}	M_{31}	M_{32}
LB spectrum	0.0515	0.0520	0.0541	0.0593	0.0472	0.0519	0.0516	0.0586
Sample number	M_{33}	M_{34}	M_{35}	M_{36}	M_{37}	M_{38}	M_{39}	M_{40}
LB spectrum	0.0614	0.0537	0.0597	0.0180	0.0593	0.0567	0.0388	0.0522

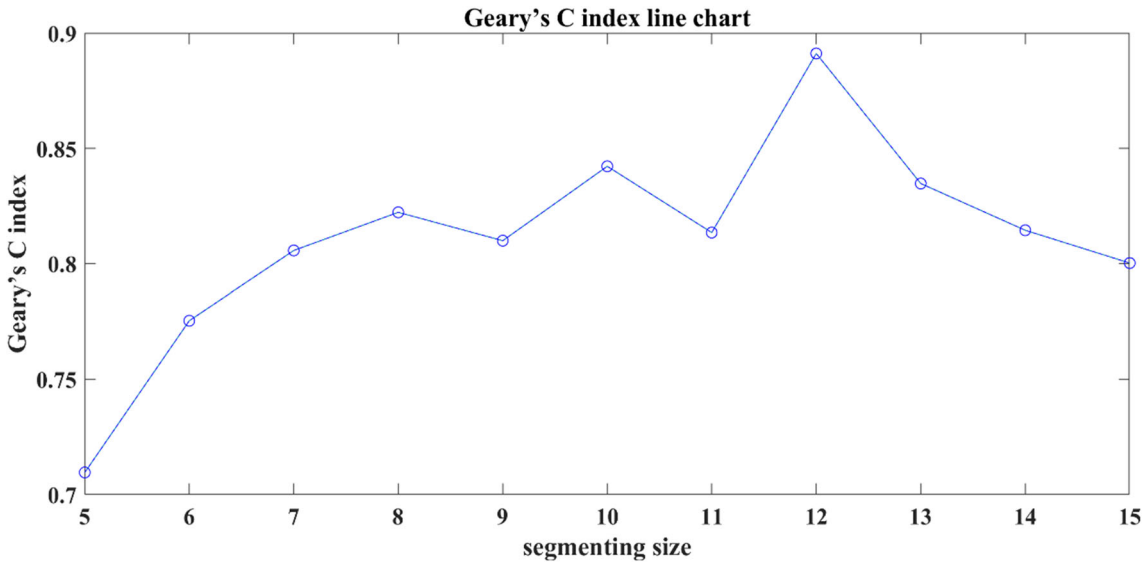

Fig. 6 Greary's C line chart of the first simulated curved surface with different segmented block sizes

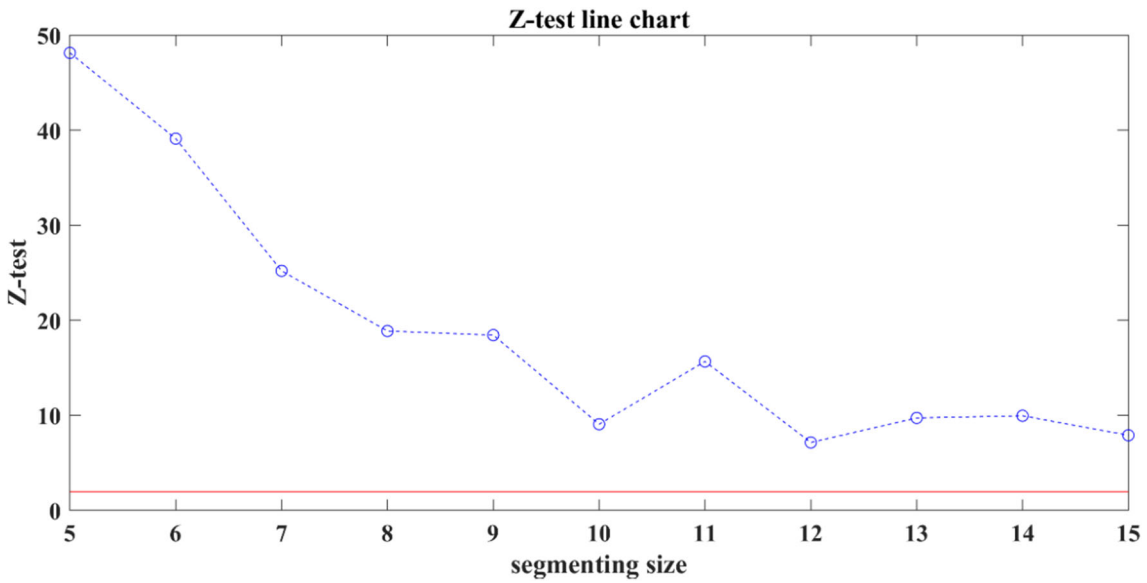

Fig. 7 Z-test line chart of a part in different segmented sizes

Table 2 Spatial geodesic clustering degree data of each surface sample

Sample number	M_1	M_2	M_3	M_4	M_5	M_6	M_7	M_8
SDCD	3.4790	3.5086	3.4836	3.6136	3.5260	3.4118	3.4495	3.5238
Sample number	M_9	M_{10}	M_{11}	M_{12}	M_{13}	M_{14}	M_{15}	M_{16}
SDCD	3.4779	3.5406	3.4460	3.5287	3.5322	3.5516	3.4292	3.5310
Sample number	M_{17}	M_{18}	M_{19}	M_{20}	M_{21}	M_{22}	M_{23}	M_{24}
SDCD	3.4969	3.4584	3.5408	3.5433	3.4628	3.5278	3.59978	3.5619
Sample number	M_{25}	M_{26}	M_{27}	M_{28}	M_{29}	M_{30}	M_{31}	M_{32}
SDCD	3.4983	3.4731	3.5293	3.5309	3.4946	3.5225	3.4356	3.5417
Sample number	M_{33}	M_{34}	M_{35}	M_{36}	M_{37}	M_{38}	M_{39}	M_{40}
SDCD	3.4695	3.4813	3.3861	3.5753	4.0981	4.2641	4.0480	4.0366

Table 3 Normality test results of curved surface simulation

	Significance level	P value	Anderson–Darling statistic	Critical value
SDCD value	0.05	0.0005	0.6368	0.7368
LB spectrum value	0.05	0.0005	0.5297	0.7368

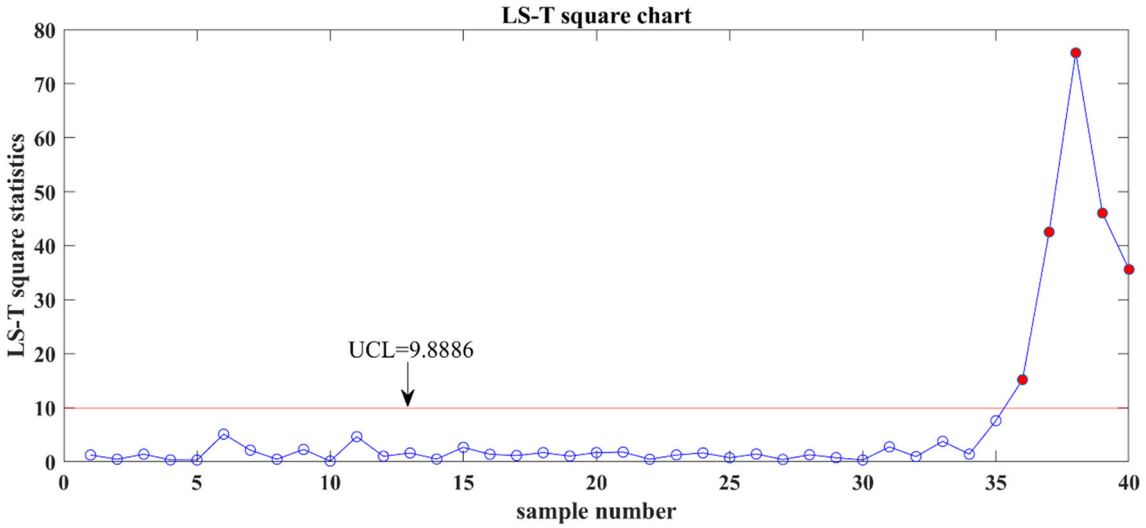

Fig. 8 LS-T^2 control chart of numerical simulation

Monitoring approaches comparison

For comparison, two methods commonly used in the past literature of curved surface profile monitoring are selected. The curved surface profile monitoring approaches proposed by Zhao and Castillo (2022) and Colosimo et al. (2014) are also applied to the same numerical simulation, which are widely used in non-Euclidean surface profile monitoring. Zhao and Castillo (2022) proposed a registration-free approach based on the Laplace–Beltrami spectrum to monitor the shape variation. The main idea is to calculate the first fifty LB spectrums of the parts, and monitoring each LB spectrum to identify part-to-part shape variation. Colosimo et al (2014) established a Gaussian process model to monitor deviations between the actual surface and the target surface. Figures 9 and 10 show the monitoring results of the DFEWMA (distribution-free multivariate exponentially weighted moving average) chart and Hotelling T^2 control chart using the approaches of Zhao and Colosimo. From Fig. 9, the upper control limit UCL is going up and down, thereby leading to the 3th curved surface is false alarm, the detective curved surfaces are alarm missing, and the control limit is extreme at the second sample. From Fig. 10, the monitoring result is extremely bad, the 4th curved surface is false alarm, and all the detective curved surfaces are mistaken as normal. According to the results of the visualization in Figs. 8, 9 and 10 among the three approaches, it is obvious that the above two approaches neither detect the curved surfaces with defects significantly, and the proposed approach can detect the small shifts of curved surface profile.

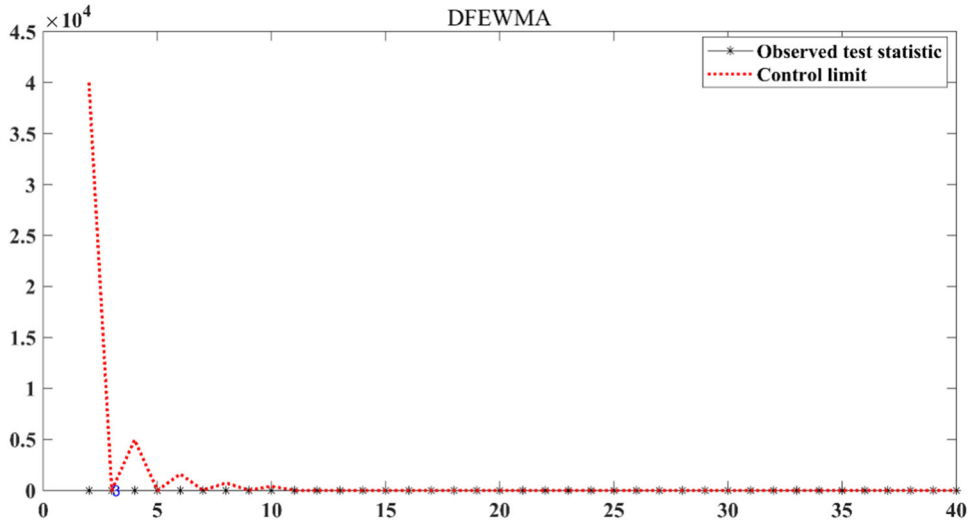

Fig. 9 **a** DFEWMA chart, **b** Enlarged view of DFEWMA chart

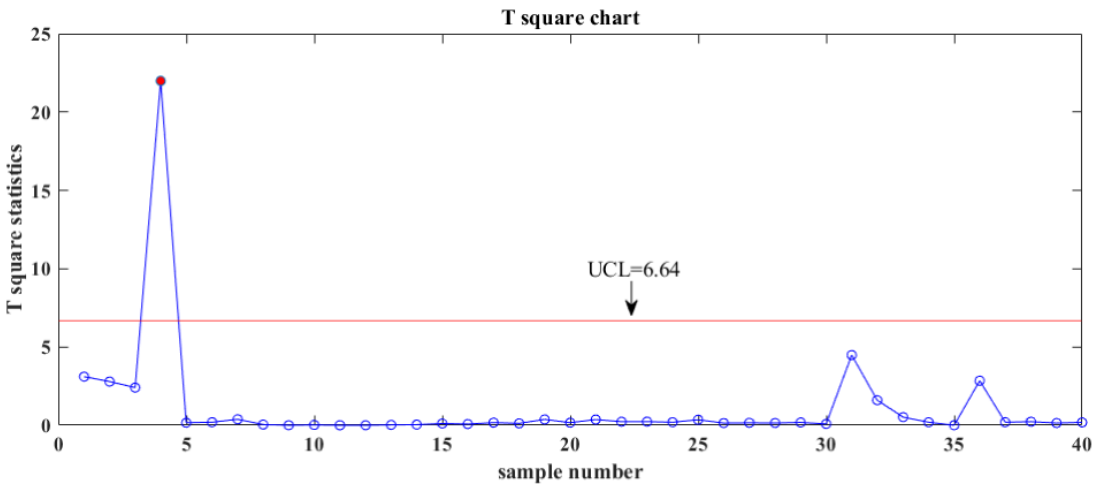

Fig. 10 Hotelling T^2 control chart obtained by Colosimo et al.

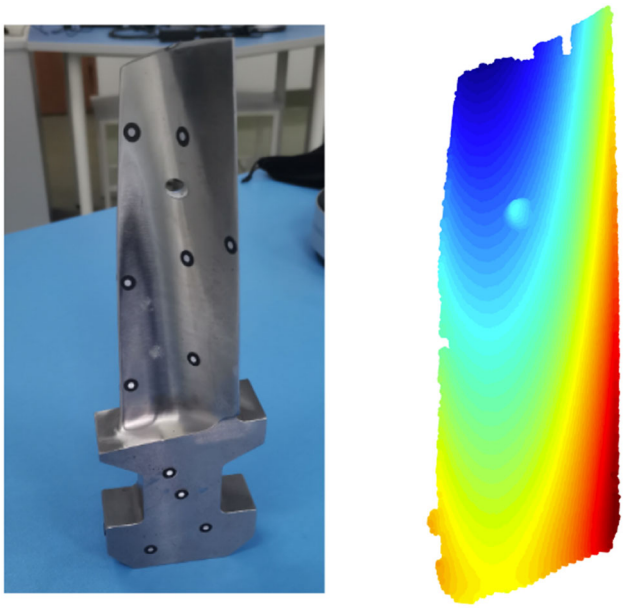

Fig. 11 **a** Blade, **b** Measured blade surface

Furthermore, in order to quantitatively evaluate the performance of various monitoring approaches, the Average Run Length (ARL) is adopted to measure of each control chart. ARL is one of evaluation indices for control chart performance and sensitivity, and it represents the average number of sample observations on the control chart from the beginning of the monitoring process until the first sample observation falls outside the control limit. When the production process is steady, the smaller ARL means the earlier fluctuations in the production process is detected, and the better performance of the control chart. There are many ways to solve the ARL, this paper chooses the Monte Carlo Method, and the exact calculation process of ARL is described as follows: Obtaining the statistics $\mathbf{T}^2_{LS}$ for each sample and control limit of the LS-Hotelling T^2 chart, since $\mathbf{T}^2_{LS}$ follows a normal distribution, then $\mathbf{T}^2_{LS}$ satisfies a Gaussian distribution with mean $\mu_{T^2_{LS}}$ and variance $\sigma_{T^2_{LS}}$. Generate 1000 random numbers using this Gaussian distribution, constructing a stochastic production process with these random numbers, repeat the above steps 1000 times. Counting the number s which exceed the control limit, the ARL can be calculated as $\frac{s}{1000}$.

The ARLs of the three approaches are calculated respectively as shown in Table 4. It is clear that the ARL of the proposed approach is the minimum, which illustrates the performance of the proposed approach is superior to the other approaches of Zhao and Colosimox in terms of monitoring accuracy and monitoring speed. Therefore, the method in this paper is more applicable to point cloud surface data than the other two methods.

Table 4 The control limit and ARL calculated by two approaches

Approach	Control limit	ARL
The proposed	9.88	1.1010
Zhao et al	–	–
Colosimo et al	6.64	2.9400

Case studies

Case study I

With the development of the fields in petrochemical, energy power and navigation, the reliability, durability and profile quality of turbine blade surface have attracted more and more attention. The blade is one of the key parts of the steam turbine. Through the steam turbine blades, the steam flow converts its own kinetic energy into the kinetic energy of the steam turbine rotor, and further converting into electrical energy by the generator set. In the manufacturing process of the blade, it includes forging ring blanks, turning inner and outer rings, wire-cutting assembly of the inner back-arc profile, milling of the back-arc profile allowance, fine milling of the back-arc profile, and polishing of the inner back-arc profile in the vapor path. Cracks, inclusions, shrinkage and other defects will appear on the surface of the steam turbine blade during these processes. The working conditions of the turbine blades are extremely harsh. The working environment temperature of the first stage blade is the highest, which is close to the inlet steam temperature. Moreover, the blade moves in the air containing a large amount of water vapor, the superheated steam will cause high temperature oxidation corrosion to the blade, which will reduce the fatigue strength of the blade. The working environment of the last stage blade belongs to the wet steam area, which is easy to produce electrochemical corrosion. In addition, due to the influence of natural cooling, a large number of water droplets are produced in the last stage area of the steam turbine. These water droplets will cause the gas density in the area to be too large, which will have a greater impact on the blades. Due to the above reasons, if the blade has a small quality problem, this defect will be gradually enlarged in the actual operation, which will cause the failure of the blade and eventually affect the safety and reliability of the steam turbine. Therefore, it is essential to guarantee the surface profile quality of the blade. The first case study is based on the turbine blade surfaces which is illustrated in Fig. 11a. The material of the turbine blade is square steel. This surface is manufactured by rough milling, semi-finish milling and finish milling. To reduce air resistance, a hole is machined to gather air and reduce the reaction force after rough milling, and it has no effect on the machining process. The whole measuring result is similar

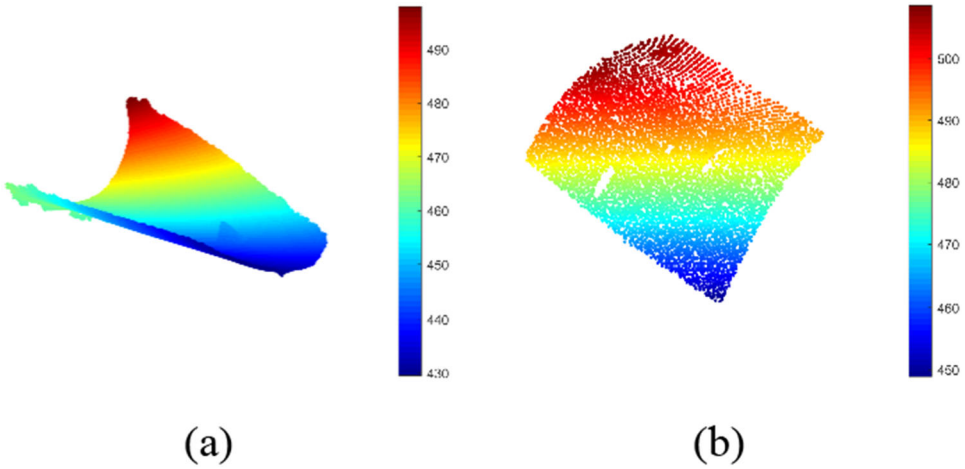

Fig. 12 **a** Measured blade point cloud, **b** Measured blade point cloud after denoising

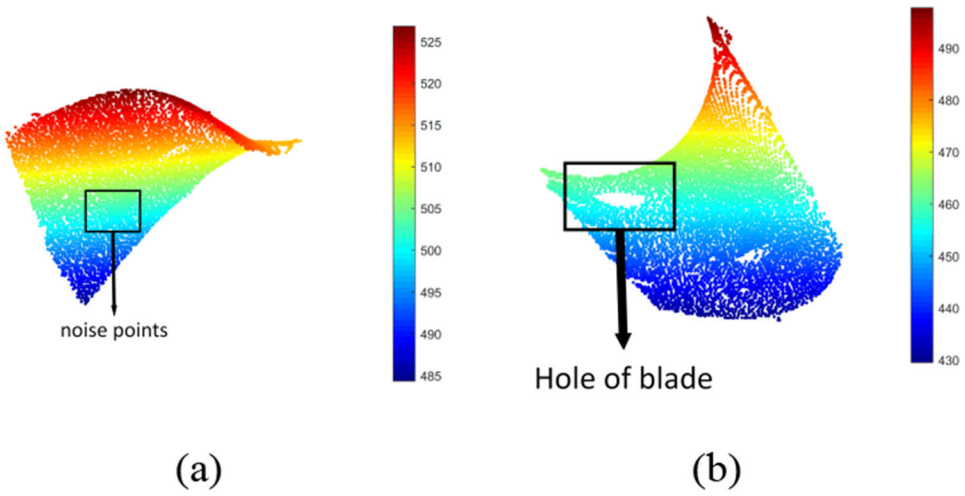

Fig. 13 **a** Defect of blade surface: noise points, **b** Defect of blade surface: hole

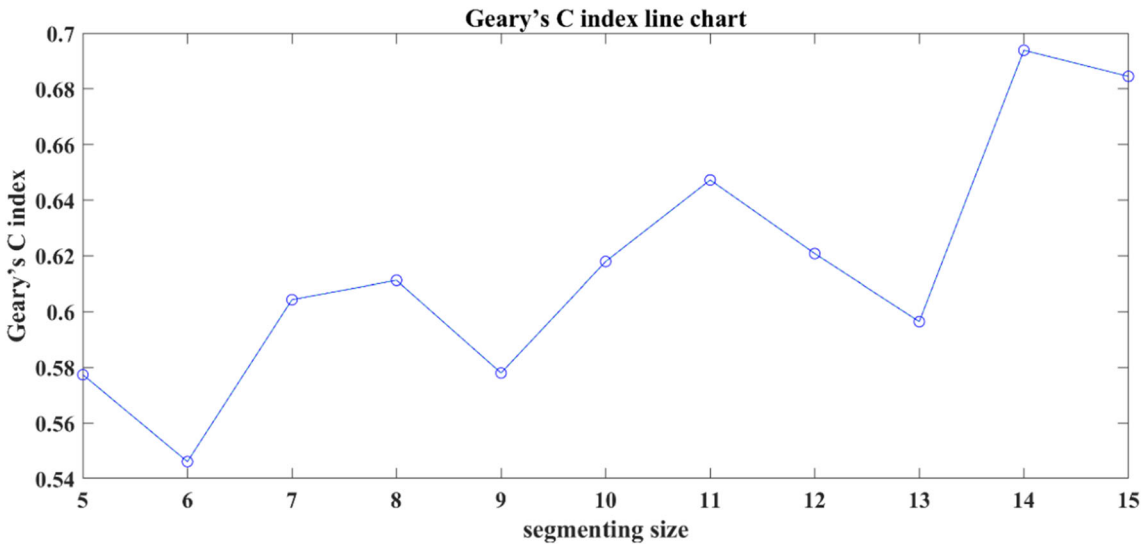

Fig. 14 Greary's C line chart of a blade surface with different segmented sizes

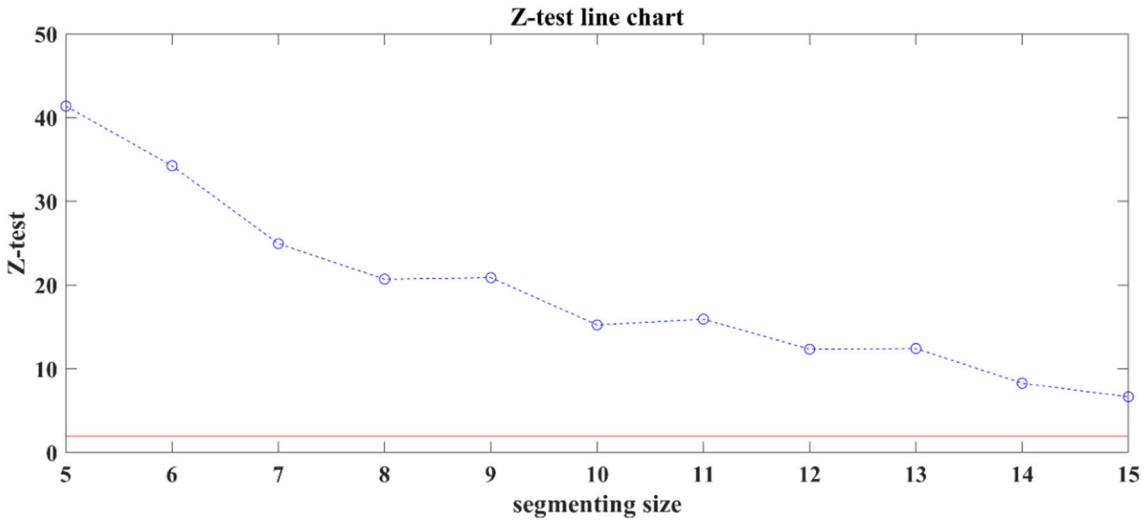

Fig. 15 Z-test line chart of a blade surface with different segmented sizes

Table 5 LB spectrum data of each blade surface sample

Sample number	P_{b1}	P_{b2}	P_{b3}	P_{b4}	P_{b5}	P_{b6}
LB spectrum	0.0105	0.0106	0.0106	0.0106	0.0106	0.0209
Sample number	P_{b7}	P_{b8}	P_{b9}	P_{b10}	P_{b11}	P_{b12}
LB spectrum	0.0208	0.0208	0.0209	0.0208	0.0210	0.0210
Sample number	P_{b13}	P_{b14}	P_{b15}	P_{b16}	P_{b17}	P_{b18}
LB spectrum	0.0209	0.0211	0.0046	0.01474	0.0147	0.0018
Sample number	P_{b19}	P_{b20}	P_{b21}	P_{b22}	P_{b23}	P_{b24}
LB spectrum	0.0018	0.0018	0.0176	0.0177	0.0178	0.0046
Sample number	P_{b25}	P_{b26}	P_{b27}	P_{b28}	P_{b29}	P_{b30}
LB spectrum	0.0169	0.0116	0.0140	0.0018	0.0002	0.0015

as Fig. 11b. Therefore, it is necessary to monitor the profile quality of the turbine blade surface. Thirty point cloud data samples of different blade surfaces are measured by the 3D laser scanning instrument. The first twenty-five blade samples ($P_{bi}|i = 1, 2, 3, ..., 25$) are manufactured in a stable and controlled production process without abnormal factors. Figure 12a shows any one of the first twenty-five blade surface samples. By adding small interference factors to make the production process out of control, the rest five blade surface samples ($P_{bi}|i = 26, 27..., 30$) are obtained. Figure 13 shows two types of defects occurred on the blade surfaces. Point cloud data denoising are performed on the measured thirty blade surface samples, and Fig. 12b shows one of the surfaces after denoising. Table 5 shows the LB spectrum of each blade surface sample.

Setting the initial segmenting size as $W \times H = 5$ mm $\times$ 5 mm, the cutoff segmenting size as 15 mm $\times$ 15 mm, and the segmenting interval $B = 1$ mm. Hence, the thirty blade surface samples are segmented as point cloud blocks $Q_n = WQ_n \times HQ_n = [5 + (n-1) \times 1] \times [5 + (n-1) \times 1]$. The spatial geodesic clustering degree is calculated for different block segmenting sizes, and Greary's C index and Z-test are calculated respectively. Figures 14 and 15 show the result of the first blade surfaces. It can be seen the optimal block size is selected as 6mm $\times$ 6mm for spatial geodesic clustering degree calculation. Repeat the above procedures for the rest blade surfaces, the optimal block size is still 6mm $\times$ 6mm. Table 6 shows the spatial geodesic clustering degree of each blade surface sample. Meantime, Table 7 shows the normality test results, the results of Anderson–Darling test show that the normality of the two variable is satisfied.

Figure 16 shows the LS-T^2 control chart constructed by the LB spectrum and the spatial geodesic clustering degree of blade surface samples. It is obvious that the defective blade surfaces are detected timely by the LS-T^2 control chart and alerting when it first appears. Therefore, the results indicate the proposed monitoring approach can accurately identify the variations of blade surface profiles, thereby being applied well for the online monitoring of turbine blade manufacturing process.

Table 6 Spatial geodesic clustering degree data of each blade surface sample

Sample number	P_{b1}	P_{b2}	P_{b3}	P_{b4}	P_{b5}	P_{b6}
SDCD	52.9183	53.5568	53.7380	53.6500	52.23409	50.51299
Sample number	P_{b7}	P_{b8}	P_{b9}	P_{b10}	P_{b11}	P_{b12}
SDCD	51.8031	53.2738	53.6960	49.6470	46.6661	47.9185
Sample number	P_{b13}	P_{b14}	P_{b15}	P_{b16}	P_{b17}	P_{b18}
SDCD	50.2300	49.7390	45.4900	52.5929	53.1806	53.8910
Sample number	P_{b19}	P_{b20}	P_{b21}	P_{b22}	P_{b23}	P_{b24}
SDCD	53.1645	49.4324	46.891	45.2623	47.3015	43.5512
Sample number	P_{b25}	P_{b26}	P_{b27}	P_{b28}	P_{b29}	P_{b30}
SDCD	48.0536	61.4525	68.8703	60.5642	56.9785	60.2942

Table 7 Normality test results of blade surface study

	Significance level	P value	Anderson–Darling statistic	Critical value
SDCD value	0.05	0.0373	0.7316	0.7811
LB spectrum value	0.05	0.0014	0.6571	1.3401

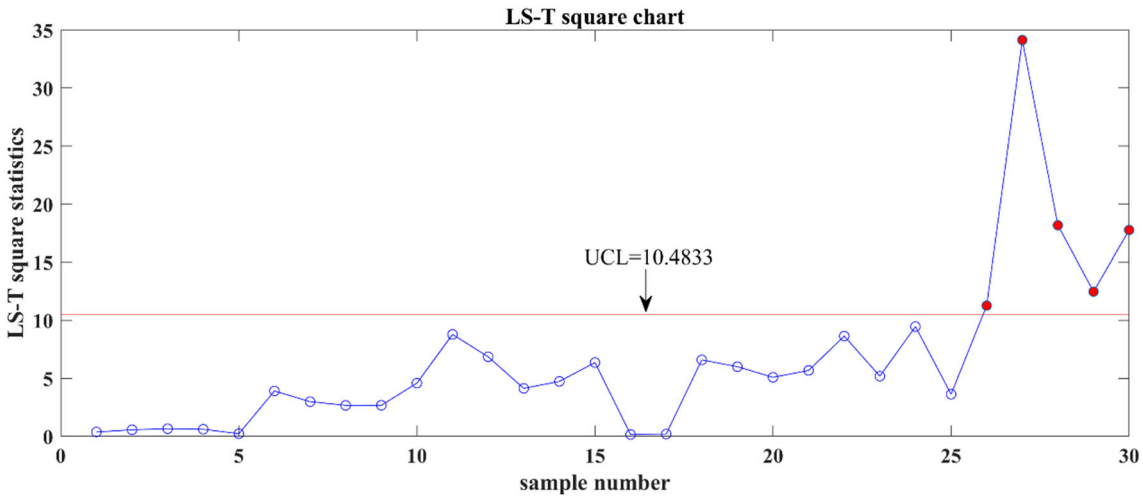

Fig. 16 Control chart of blade surface

Case study II

The inner surface of the cylinder head combustion chamber is a complex three-dimensional surface which is cast from a mold. The cylinder head is one of the most critical parts of the engine. The shape and internal structure of the engine cylinder head are complex. It has the characteristics of multi-cavity and intersecting holes. The surface curvature and wall thickness change dramatically, and the forming consistency is poor. The cylinder head has an important influence on the service performance and reliability of the engine. There are many processing procedures and complex processes, and the strict requirements of the manufacturing errors. The processing of cylinder head mainly includes casting, rough milling, semi-finishing milling, finishing milling and so on. Firstly, the inner surface of the cylinder head combustion chamber is obtained by casting. Due to long-term contact with the casting material at high temperatures, the mold easily wears which affects the combustion chamber surface shape. Then the bottom surface of the cylinder head is machined by rough milling, semi-finishing milling and finishing milling, and the volume of the combustion chamber is controlled by the milling depth. Milling process will produce burrs, scratches and other defects on the surface of the engine cylinder head combustion chamber. Moreover, the difference of milling depths among cylinders will lead to poor consistency of combustion chamber surface forming and fluctuation of surface profile quality, thereby affecting the performance of the engine. The second case study is based on a surface of cylinder head combustion chamber which is illustrated in Fig. 17a. The material of the cylinder head combustion cham-

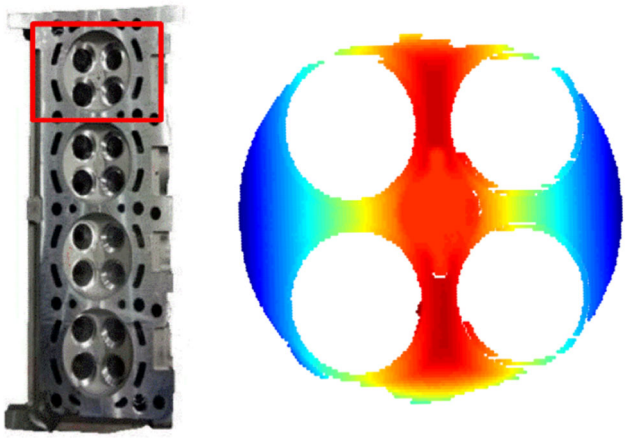

(a) (b)

Fig. 17 **a** Cylinder head combustion chamber, **b** Measured cylinder head combustion chamber

ber is Cast iron FC250. This surface is a major sealing surface in automotive powertrain and the measuring result is shown Fig. 17b.

Thirty raw point cloud data of the cylinder head combustion chamber surfaces can be obtained by the 3D laser scanning instrument. The cylinder heads are produced in a stable and controlled production process and free from accidental influences. The controlled cylinder head samples can be obtained as $P_{ci}|i = 1, 2, 3, \ldots 30$. Figure 18a shows any one of the combustion chamber surface samples. Point cloud data denoising are performed on the combustion chamber surface samples, and Fig. 18b shows the corresponding combustion chamber surface samples after point cloud data denoising.

Calculated the LB spectrum value and spatial geodesic clustering degree value for these thirty combustion chamber surfaces data. Table 8 shows LB spectrum values for each combustion chamber surface.

Setting the initial segmenting size as $W \times H = 1\text{mm} \times 1\text{mm}$, the segmenting interval $B = 2\text{mm}$, and the cutoff segmenting size as $15\text{mm} \times 15\text{mm}$. Hence, the thirty combustion chamber surface samples are segmented as point cloud blocks $Q_n = WQ_n \times HQ_n = [5+(n-1)\times 2] \times [5+(n-1)\times 2]$, and calculate the corresponding spatial geodesic clustering degree for different block segmenting sizes. Greary's C index and Z-test are calculated respectively, Figs. 19 and 20 show the result of the combustion chamber surface samples. It can be seen the optimal block size is selected as $1\text{mm} \times 1\text{mm}$ for spatial geodesic clustering degree calculation.

Repeat the above procedures for the rest blade surfaces, the optimal block size is still $1\text{mm} \times 1\text{mm}$, and Table 9 shows spatial geodesic clustering degree for each combustion chamber surface. Meantime, Table 10 shows the normality test results, the results of Anderson–Darling test show that the normality of the two variable is satisfied.

Figure 21 shows the LS-T^2 control chart constructed by using the LB spectrum and spatial geodesic clustering degree values of the combustion chamber surfaces, and it can be seen that there are no out-of-control surfaces. Therefore, the results indicate the proposed monitoring approach has a high control limit, which can effectively avoid the false alarm of combustion chamber surface profiles, thereby being a powerful tool for in-control combustion chamber manufacturing process monitoring.

Conclusions

In this paper, a novel curved surface profile monitoring approach based on geometrical-spatial joint features is proposed. The Laplace–Beltrami spectrum is developed to characterize the shape information of the curved surface, and it is an inherent measure of the three-dimensional curved surface manifold which does not change with the rigidity of the parts or the change of environmental coordinates. A new method of extracting point cloud distribution features is proposed, which overcomes the drawbacks of the representation local distribution information of the point cloud in traditional density extraction methods. The feature is called the spatial geodesic clustering degree, which represents all the spatial distributions information of the curved surface and performs well in both the density and randomness of the point cloud distribution. Laplace–Beltrami spectrum and spatial geodesic clustering degree are constructed to establish the LS-Hotelling T^2 control chart and realize curved surface monitoring. The proposed monitoring approach takes full advantage of the entire wealth information on the high-density point clouds and can detect the small shifts of non-Euclidean curved surfaces. The effectiveness of the proposed monitoring approach is validated by the numerical simulation and real-world engineering surfaces case studies. The proposed approach can achieve non-Euclidean surface profile monitoring and identify the stability of the manufacturing process, which can provide strong technical support for ensuring the manufacturing process quality. However, the monitoring scheme in this paper is based on the Hotelling T^2 control chart, it is possible to design a control chart suitable for various probability distribution of part quality characteristic data, which is one of the next research directions.

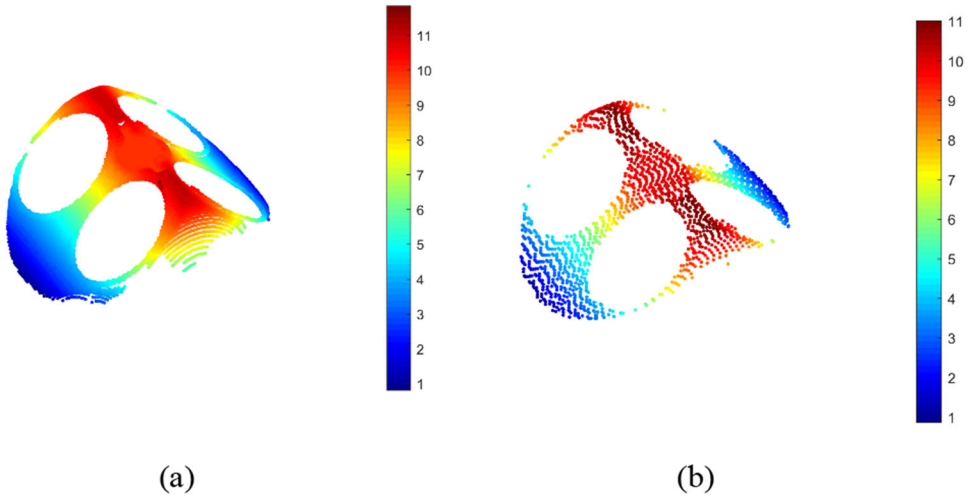

Fig. 18 **a** Normal combustion chamber surface, **b** combustion chamber surface after denoising

Table 8 LB spectrum data of each combustion chamber surface sample

Sample number	P_{c1}	P_{c2}	P_{c3}	P_{c4}	P_{c5}	P_{c6}
LB spectrum	0.0258	0.0261	0.0264	0.0096	0.0454	0.0422
Sample number	P_{c7}	P_{c8}	P_{c9}	P_{c10}	P_{c11}	P_{c12}
LB spectrum	0.0109	0.0109	0.0454	0.0423	0.0518	- 9.6838E-19
Sample number	P_{c13}	P_{c14}	P_{c15}	P_{c16}	P_{c17}	P_{c18}
LB spectrum	0.0499	0.0511	0.0123	0.0110	0.0257	0.0124
Sample number	P_{c19}	P_{c20}	P_{c21}	P_{c22}	P_{c23}	P_{c24}
LB spectrum	0.0261	0.0109	0.0472	0.0508	0.0506	0.0518
Sample number	P_{c25}	P_{c26}	P_{c27}	P_{c28}	P_{c29}	P_{c30}
LB spectrum	0.0504	0.0107	0.0471	0.0471	0.0470	0.0482

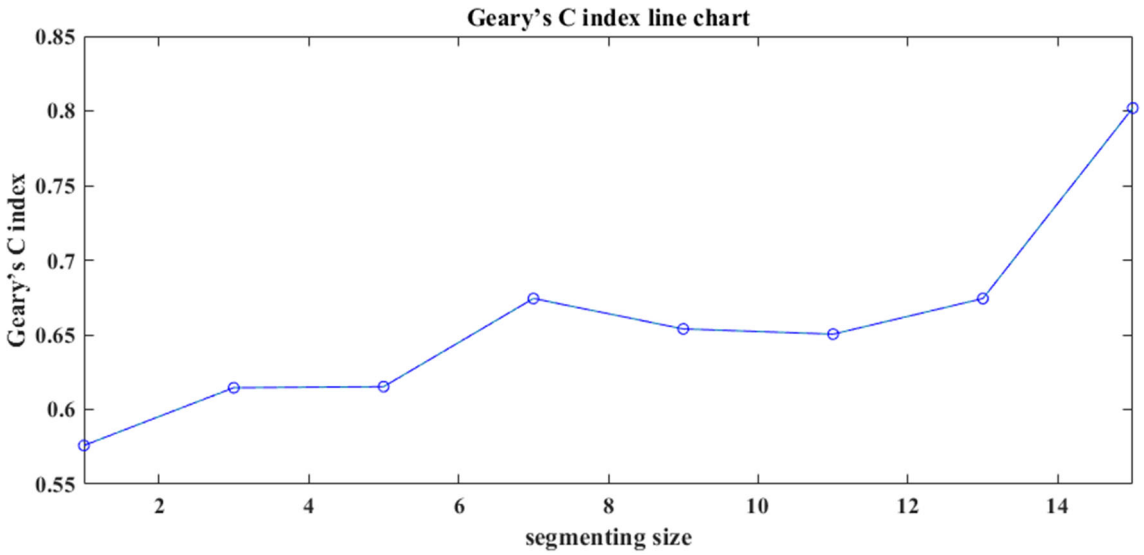

Fig. 19 Greary's C line chart of a combustion chamber surface with different segmented sizes

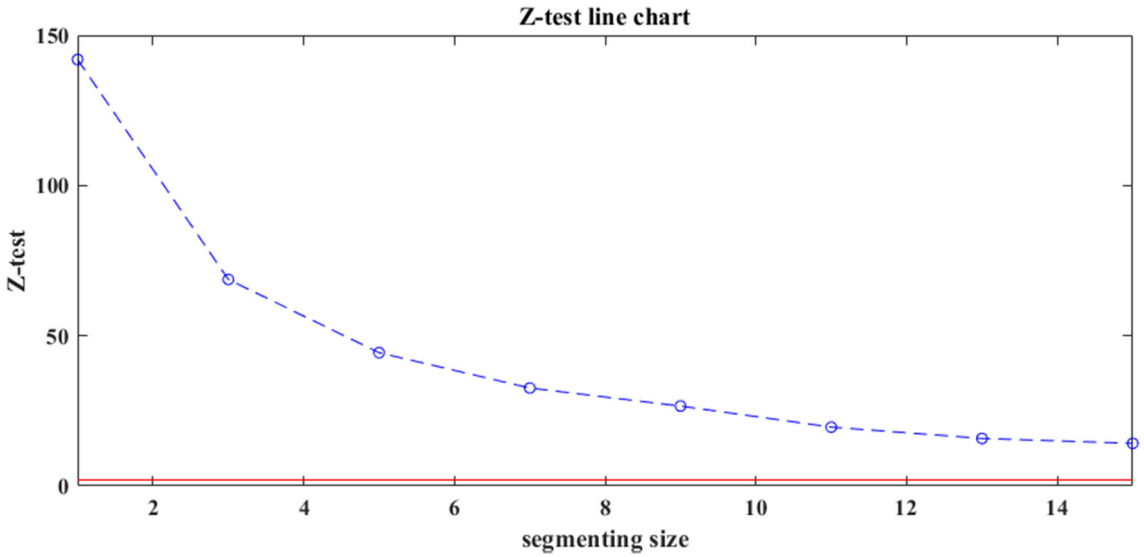

Fig. 20 Z-test line chart of a combustion chamber surface with different segmented sizes

Table 9 Spatial geodesic clustering degree data of each combustion chamber surface sample

Sample number	P_{c1}	P_{c2}	P_{c3}	P_{c4}	P_{c5}	P_{c6}
SDCD	2.3687	2.2253	2.1680	2.3952	2.1623	2.1376
Sample number	P_{c7}	P_{c8}	P_{c9}	P_{c10}	P_{c11}	P_{c12}
SDCD	2.2853	2.2711	2.1245	2.1285	2.1201	2.2910
Sample number	P_{c13}	P_{c14}	P_{c15}	P_{c16}	P_{c17}	P_{c18}
SDCD	2.2699	2.1638	2.1934	2.2859	2.3158	2.2420
Sample number	P_{c19}	P_{c20}	P_{c21}	P_{c22}	P_{c23}	P_{c24}
SDCD	2.2356	2.2556	2.2856	2.2464	2.2636	2.1155
Sample number	P_{c25}	P_{c26}	P_{c27}	P_{c28}	P_{c29}	P_{c30}
SDCD	2.2890	2.3171	2.3873	2.3030	2.3894	2.0963

Table 10 Normality test results of combustion chamber surface study

	Significance level	P value	Anderson–Darling statistic	Critical value
SDCD value	0.05	0.1752	0.5193	0.6315
LB spectrum value	0.05	0.0005	0.7316	2.0842

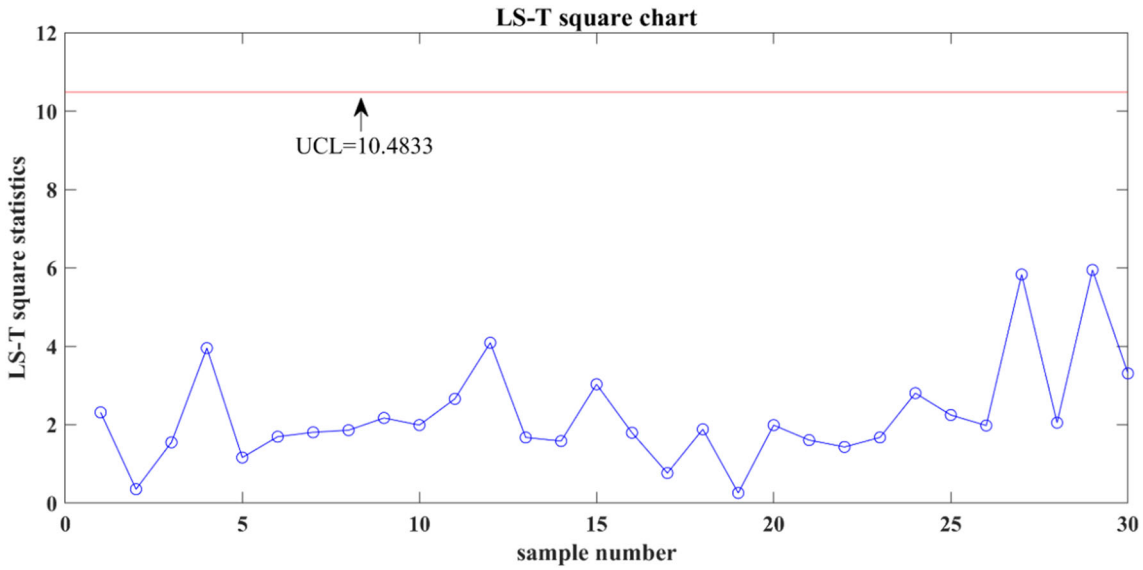

Fig. 21 Control chart of combustion chamber surface

Acknowledgements This work is supported by Natural Science Foundation of Zhejiang Province (Grant No. LQ22E050017), Zhejiang Science and Technology Plan Project (Grant No. 2018C01003), National Natural Science Foundation of China (Grant No. 52275499), and National Key Research and Development Program of China (Grant No. 2022YFF0605700).

Author contributions Yiping Shao contributed to propose ideas and methods, conduct experimental verification, and write the manuscript. Jun Chen contributed to data collection, method validation, and write the manuscript. Xiaoli Gu contributed to method investigation and visualization. Jiansha Lu contributed to propose ideas, supervise method, manuscript reviewing and checking. Shichang Du supervises methods, funding acquisition, and project administration. All authors have read and agreed to the published version of the manuscript.

Funding This work is funded by Natural Science Foundation of Zhejiang Province (Grant No. LQ22E050017), Zhejiang Science and Technology Plan Project (Grant No. 2018C01003), National Natural Science Foundation of China (Grant No. 52275499), and National Key Research and Development Program of China (Grant No. 2022YFF0605700).

Data availability The authors declare that all data presented in this article are available.

Declarations

Competing interests The authors have no competing interests to declare that are relevant to the content of this article.

References

Baek, J., Jeong, M. K., & Elsayed, E. A. (2023). Monitoring variations in multimode surface topography. *International Journal of Production Research, 61*(4), 1129–1145. https://doi.org/10.1080/00207543.2022.2027539

Bui, A. T., & Apley, D. W. (2022a). Analyzing nonparametric part-to-part variation in surface point cloud data. *Technometrics, 64*(4), 457–474. https://doi.org/10.1080/00401706.2021.1883482

Bui, A. T., & Apley, D. W. (2022b). Robust monitoring of stochastic textured surfaces. *International Journal of Production Research, 60*(16), 5071–5086. https://doi.org/10.1080/00207543.2021.1949642

Colosimo, B. M., Cicorella, P., Pacella, M., & Blaco, M. (2014). From profile to surface monitoring: SPC for cylindrical surfaces via gaussian processes. *Journal of Quality Technology, 46*(2), 95–113. https://doi.org/10.1080/00224065.2014.11917956

Dastoorian, R., & Wells, L. J. (2023). A hybrid off-line/on-line quality control approach for real-time monitoring of high-density datasets. *Journal of Intelligent Manufacturing, 34*(2), 669–682. https://doi.org/10.1007/s10845-021-01818-8

He, D., Xu, K., & Zhou, P. (2019). Defect detection of hot rolled steels with a new object detection framework called classification priority network. *Computers & Industrial Engineering, 128*, 290–297. https://doi.org/10.1016/j.cie.2018.12.043

He, Z., Zuo, L., Zhang, M., & Megahed, F. M. (2016). An image-based multivariate generalized likelihood ratio control chart for detecting and diagnosing multiple faults in manufactured products. *International Journal of Production Research, 54*(6), 1771–1784. https://doi.org/10.1080/00207543.2015.1062569

Huang, T. T., Wang, S. G., Yang, S. K., & Dai, W. (2021). Statistical process monitoring in a specified period for the image data of fused deposition modeling parts with consistent layers. *Journal of Intlligent Manufacturing, 32*(8), 2181–2196. https://doi.org/10.1007/s10845-020-01628-4

Jiang, X. J., Senin, N., Scott, P. J., & Blateyron, F. (2021). Feature-based characterisation of surface topography and its application. *CIRP Journal of Manufacturing Science and Technology, 70*(2), 681–702. https://doi.org/10.1016/j.cirp.2021.05.001

Li, Y., Liu, Y. H., Wang, J. L., Wang, Y., & Tian, Y. B. (2022). Real-time monitoring of silica ceramic composites grinding surface roughness based on signal spectrum analysis. *Ceramics International, 48*(5), 7204–7217. https://doi.org/10.1016/j.ceramint.2021.11.281

Li, Y., Pei, D., & Wu, Z. (2020). A multivariate non-parametric control chart based on run test. *Computers & Industrial Engineering, 149*, 106839. https://doi.org/10.1016/j.cie.2020.106839

Megahed, F. M., Wells, L. J., Camelio, J. A., & Woodall, W. H. (2012). A spatiotemporal method for the monitoring of image data. *Quality and Reliability Engineering International, 28*(8), 967–980. https://doi.org/10.1002/qre.1287

Moreira, L. C., Li, W. D., Lu, X., & Fitzpatrick, M. E. (2019). Supervision controller for real-time surface quality assurance in CNC machining using artificial intelligence. *Computers & Industrial Engineering, 127*, 158–168. https://doi.org/10.1016/j.cie.2018.12.016

Ren, J. Y., & Ni, D. (2021). A real-time monitoring framework for wafer fabrication processes with run-to-run variations. *IEEE Transanctions on Semiconductor Manufacturing, 34*(4), 483–492. https://doi.org/10.1109/TSM.2021.3104101

Shang, Y., Li, T., Song, L., & Wang, Z. (2019). Control charts for monitoring two-dimensional spatial count data with spatial correlations. *Computers & Industrial Engineering, 137*, 106043. https://doi.org/10.1016/j.cie.2019.106043

Shao, Y., Du, S. C., & Tang, H. T. (2021). An extended bi-dimensional empirical wavelet transform based filtering approach for engineering surface separation using high definition metrology. *Measurement, 178*, 109259. https://doi.org/10.1016/j.measurement.2021.109259

Suriano, S., Wang, H., Shao, C., Hu, S. J., & Sekhar, P. (2015). Progressive measurement and monitoring for multi-resolution data in surface manufacturing considering spatial and cross correlations. *IIE Transactions, 47*(10), 1033–1052. https://doi.org/10.1080/0740817X.2014.998389

Wang, A., Wang, K., & Tsung, F. (2014). Statistical surface monitoring by spatial-structure modeling. *Journal of Quality Technology, 46*(4), 359–376. https://doi.org/10.1080/00224065.2014.11917977

Wang, K., Jiang, W., & Li, B. (2016). A spatial variable selection method for monitoring product surface. *International Journal of Production Research, 54*(14), 4161–4181. https://doi.org/10.1080/00207543.2015.1109723

Wang, K., & Tsung, F. (2005). Using profile monitoring techniques for a data-rich environment with huge sample size. *Quality and Reliability Engineering International, 21*(7), 677–688. https://doi.org/10.1002/qre.711

Wells, L. J., Dastoorian, R., & Camelio, J. A. (2021). A novel NURBS surface approach to statistically monitor manufacturing processes with point cloud data. *Journal of Intelligent Manufacturing, 32*(2), 329–345. https://doi.org/10.1007/s10845-020-01574-1

Wells, L. J., Shafae, M. S., & Camelio, J. A. (2016). Automated surface defect detection using high-density data. *Journal of Manufacturing Science and Engineering of ASME, 138*(7), 071001. https://doi.org/10.1115/1.4032391

Zhang, F., Zhang, J., & Ma, J. (2023). Data-manifold-based monitoring and anomaly diagnosis for manufacturing process. *Journal of Intelligent Manufacturing, 34*(7), 3159–3177. https://doi.org/10.1007/s10845-022-01978-1

Zhang, L., Wang, K., & Chen, N. (2016). Monitoring wafers' geometric quality using an additive Gaussian process model. *IIE Transactions, 48*(1), 1–15. https://doi.org/10.1080/0740817x.2015.1027455

Zhao, C., Du, S., Deng, Y., Li, G., & Huang, D. (2020). Circular and cylindrical profile monitoring considering spatial correlations. *Journal of Manufacturing Systems, 54*, 35–49. https://doi.org/10.1016/j.jmsy.2019.11.011

Zhao, C., Du, S., Lv, J., Deng, Y., & Li, G. (2023a). A novel parallel classification network for classifying three-dimensional surface with point cloud data. *Journal of Intelligent Manufacturing, 34*(2), 515–527. https://doi.org/10.1007/s10845-021-01802-2

Zhao, X., & del Castillo, E. D. (2021). An intrinsic geometrical approach for statistical process control of surface and manifold data. *Technometrics, 63*(3), 295–312. https://doi.org/10.1080/00401706.2020.1772114

Zhao, X., & Castillo, E. D. (2022). A registration-free approach for statistical process control of 3D scanned objects via FEM. *Precision Engineering, 74*, 247–263. https://doi.org/10.1016/j.precisioneng.2021.10.018

Zhao, C., Lui, C. F., Du, S., Wang, D., & Shao, Y. (2023b). An earth mover's distance based multivariate generalized likelihood ratio control chart for effective monitoring of 3D point cloud surface. *Computers & Industrial Engineering, 175*, 108911. https://doi.org/10.1016/j.cie.2022.108911

Publisher's Note Springer Nature remains neutral with regard to jurisdictional claims in published maps and institutional affiliations.

Springer Nature or its licensor (e.g. a society or other partner) holds exclusive rights to this article under a publishing agreement with the author(s) or other rightsholder(s); author self-archiving of the accepted manuscript version of this article is solely governed by the terms of such publishing agreement and applicable law.